TOI-257b (HD 19916b)

Addison, Brett C.; Wright, Duncan J.; Nicholson, Belinda A.; Cale, Bryson; Mocnik, Teo; Huber, Daniel; Plavchan, Peter; Wittenmyer, Robert A.; Vanderburg, Andrew; Chaplin, William J.; Chontos, Ashley; Clark, Jake T.; Eastman, Jason D.; Ziegler, Carl; Brahm, Rafael; Carter, Bradley D.; Clerte, Mathieu; Espinoza, Néstor; Horner, Jonathan; Bentley, John

DOI:
10.1093/mnras/staa3960

MNRAS 000, 1–21 (2020) Preprint 22 January 2020 Compiled using MNRAS LATEX style file v3.0

TOI-257b (HD 19916b): A Warm sub-Saturn on a Moderately Eccentric Orbit Around an Evolved F-type Star

Brett C. Addison,[1]★ Duncan J. Wright,[1] Belinda A. Nicholson,[2,1] Bryson Cale,[3] Teo Mocnik,[4] Daniel Huber,[5] Peter Plavchan,[3] Robert A. Wittenmyer,[1] Andrew Vanderburg,[6,7] William J. Chaplin,[8,9] Ashley Chontos,[5,10] Jake T. Clark, [1] Jason D. Eastman,[11] Carl Ziegler,[12] Rafael Brahm,[13,14,15] Bradley D. Carter,[1] Mathieu Clerte,[1] Néstor Espinoza,[16] Jonathan Horner,[1] John Bentley,[33] Stephen R. Kane,[4] John F. Kielkopf,[18] Emilie Laychock,[19] Matthew W. Mengel,[1] Jack Okumura,[1] Keivan G. Stassun,[20,21] Timothy R. Bedding,[22,9] Brendan P. Bowler,[6] Andrius Burnelis,[24] Michaela Collins,[19] Ian Crossfield,[25,26] Allen B. Davis,[27] Dag Evensberget,[1] Alexis Heitzmann,[1] Steve B. Howell,[28] Nicholas Law,[29] Andrew W. Mann,[29] Stephen Marsden,[1] James O'Connor,[1] Avi Shporer,[31] Catherine Stevens,[24] C.G. Tinney,[33] Christopher Tylor,[1] Songhu Wang,[27,34] Hui Zhang,[35] Thomas Henning,[36] Diana Kossakowski,[36] George Ricker,[31] Paula Sarkis,[36] Roland Vanderspek,[31] David W. Latham,[37] Sara Seager,[31,38] Joshua N. Winn,[39] Jon M. Jenkins,[40] Ismael Mireles,[31] Pam Rowden,[41] Joshua Pepper,[42] Tansu Daylan,[31,32] Joshua E. Schlieder,[43] Karen A. Collins,[11] Kevin I. Collins,[3] Thiam-Guan Tan,[44] Warrick H. Ball,[8,9] Sarbani Basu,[27] Derek L. Buzasi,[46] Tiago L. Campante,[47,48] Enrico Corsaro,[49] Lucía González-Cuesta,[50,51] Guy R. Davies,[8,9] Rafael A. García,[53,54] Zhao Guo,[55] Rasmus Handberg,[9] Saskia Hekker,[56,9] Daniel R. Hey,[22,9] Thomas Kallinger,[57] Steven D. Kawaler,[58] Cenk Kayhan,[59] James S. Kuszlewicz,[56,9] Mikkel N. Lund,[9] Alexander Lyttle,[8,9] Savita Mathur,[50,51] Andrea Miglio,[8,9] Benoit Mosser,[60] Martin B. Nielsen,[8,9,45] Aldo M. Serenelli,[61,62] Victor Silva Aguirre,[9] & Nathalie Themeßl[56,9]

The authors' affiliations are shown in Appendix B.

Accepted XXX. Received YYY; in original form ZZZ

ABSTRACT

We report the discovery of a warm sub-Saturn, TOI-257b (HD 19916b), based on data from NASA's Transiting Exoplanet Survey Satellite (*TESS*). The transit signal was detected by *TESS* and confirmed to be of planetary origin based on radial-velocity observations with the Minerva-Australis telescope array. An analysis of the *TESS* photometry, the Minerva-Australis, FEROS, and HARPS radial velocities, and the asteroseismic data of the stellar oscillations reveals that TOI-257b has a mass of $M_P = 0.134^{+0.023}_{-0.022}$ M$_J$ ($42.6^{+7.3}_{-7.0}$ $M_\oplus$), a radius of $R_P = 0.626^{+0.013}_{-0.012}$ R$_J$ ($7.02^{+0.15}_{-0.13}$ $R_\oplus$), and an orbit with eccentricity $0.242^{+0.040}_{-0.065}$ and period 18.38827 ± 0.00072 days. TOI-257b orbits a bright (V = 7.570 mag) somewhat evolved late F-type star with $M_* = 1.390 \pm 0.046$ M$_{sun}$, $R_* = 1.888 \pm 0.033$ R$_{sun}$, $T_{eff} = 6075 \pm 90$ K, and $v \sin i = 11.3 \pm 0.5$ km s^{-1}. Additionally, we statistically validate a second non-transiting sub-Saturn mass planet on a $\sim$ 71 day orbit using the radial velocity data. This system joins the ranks of a small number of exoplanet host stars that have been characterized with asteroseismology. Warm sub-Saturns are rare in the known sample of exoplanets, and thus the discovery of TOI-257b is important in the context of future work studying the formation and migration history of similar planetary systems.

Key words: planetary systems – techniques: radial velocities – techniques: photometric – techniques: spectroscopic – asteroseismology – stars: individual (TIC 200723869/TOI-257)

1 INTRODUCTION

When Mayor & Queloz (1995) announced the discovery of the first hot Jupiter, 51 Pegasi b, astronomers were baffled by the existence of a Jovian planet orbiting its host star with such a short orbital period (about 4.2 days). That discovery revolutionized our understanding of the planet formation process, revealing the situation to be more complex than had been expected based on studies of the Solar system (e.g., Lissauer 1993). Radial velocity and transit surveys over the past two decades have uncovered numerous warm and hot giant exoplanets with orbital periods shorter than 100 days (see, e.g., Butler et al. 1997; Bayliss et al. 2013; Brahm et al. 2016; Van Eylen et al. 2018; Dawson et al. 2019; Kipping et al. 2019), and occurrence studies based on those discoveries suggest that such planets can be found orbiting $\sim$ 1% of all Sun-like stars (e.g., Howard et al. 2010, 2012; Wright et al. 2012; Zhou et al. 2019) (in comparison to an occurrence rate of at least 7% for more distant planets; see, e.g., Foreman-Mackey et al. 2016; Wittenmyer et al. 2020).

In addition to the Solar System lacking a hot Jupiter, it also lacks other broad classes of planets such as super-Earths and mini-

★ E-mail: Brett.Addison@usq.edu.au

Neptunes ($\sim 1.5-3\,R_\oplus$) as well as planets larger than Neptune and smaller than Saturn, known as sub-Saturns (which we have defined as planets with a radius between $\sim 5-8\,R_\oplus$). Despite the lack of sub-Saturns in the Solar System, they appear to be nearly twice as common as Jovians ($\sim 8-24\,R_\oplus$) for orbital periods between $5-100$ days, which are surprisingly rare around solar type stars (2.9% for sub-Saturns versus 1.6% for Jovians, Petigura et al. 2013).

Sub-Saturns are a key class of planets to study for understanding the formation, migration, and compositions of giant planets in general. Their large size requires a significant H/He envelope that comprises a majority of their planetary volume, yet their masses are sufficiently small that their cores are not degenerate (unlike for planets near the mass of Jupiter). This means that modeling the interiors of sub-Saturns can be simplified as a planet consisting of a high-density core surrounded by thick H/He envelope and where measurements of mass and radius provide a unique solution for the planet's core and envelope mass fraction (e.g. Weiss & Marcy 2014; Petigura et al. 2016; Pepper et al. 2017; Petigura et al. 2017).

It is commonly thought that close-in giant planets, such as hot/warm Jupiters and sub-Saturns, do not form *in situ*, but instead originate beyond the protostellar ice line (typically located at several astronomical units from the host star) where there is sufficient solid material available to build up $\sim 5-20 M_\oplus$ cores (Pollack et al. 1996; Weidenschilling 2005; Rafikov 2006). In the case of Jovian planets, once their cores reach this critical mass regime, they begin to rapidly accrete gas from the protoplanetary disk to form their gaseous envelopes. This process continues until the disk is dispersed (Rafikov 2006; Tanigawa & Ikoma 2007), resulting in Jupiter-sized planets with masses of $\sim 100-10,000\,M_\oplus$. For sub-Saturns, however, the runaway accretion of gas appears to either not have occurred at all or did occur but in a gas-depleted disk (Lee et al. 2018). As a result, sub-Saturns have masses that range from ~ 10 to $100\,M_\oplus$. The mass of a sub-Saturn is strongly correlated with the metallicity of its host star, but is uncorrelated with the resulting radial size (Petigura et al. 2017).

The sample of measurements for longer period 'warm' giants and sub-Saturns thus far is small. The detection of more of these systems is then important to better constrain the formation and migration mechanisms of close-in planets.

One such source of warm giant planetary systems is NASA's *Transiting Exoplanet Survey Satellite* (*TESS*, Ricker et al. 2015), launched on 18th April, 2018. As of 6th November, 2019, the *TESS* mission has delivered a total of 1361 planetary candidates – objects that require further observations from ground-based facilities to confirm the existence of the candidate exoplanets[1]. To date, such follow-up observations have resulted in a total of 34 confirmed planetary discoveries (e.g. Nielsen et al. 2019; Vanderburg et al. 2019; Quinn et al. 2019; Wang et al. 2019) – and it is likely that many more planets will be confirmed in the months to come.

During its initial two-year primary mission, *TESS* is expected to discover several dozen warm Jupiters, Saturns, and sub-Saturns orbiting bright ($V < 10$ mag) stars (Sullivan et al. 2015; Barclay et al. 2018; Huang et al. 2018). Those planets will be ideal targets for follow-up observations to measure their masses, through radial velocity measurements, to probe their atmospheric compositions, through transmission and emission spectroscopy, and to determine their spin-orbit angles through measurements of the Rossiter-McLaughlin effect.

In this work, we report the discovery of one such planet, TOI-257b (HD 19916b and TIC 200723869), based on photometric data obtained by *TESS*, and follow-up observations using the Minerva-Australis facility at the University of Southern Queensland's Mt. Kent Observatory (Wittenmyer et al. 2018; Addison et al. 2019). The Minerva-Australis facility is an array of five independently operated 0.7 m CDK700 telescopes located at the Mount Kent Observatory in Queensland, Australia (see, Addison et al. 2019, for a detailed description of the facility). Designed as a robotic observatory, instruments are remotely accessible and can be operated both in manual or automatic configurations. Four of the telescopes in the array (T1, T3, T4, T5) simultaneously feed stellar light to a single KiwiSpec R4-100 high-resolution spectrograph via fiber optic cables. The details of the spectrograph and spectroscopic observations are provided in Section 2.3.

In Section 2 we describe the *TESS* photometric data, and the reduction of the Minerva-Australis spectroscopic data and the radial velocity pipeline, as well as radial velocities collected with other instruments. Section 3 presents the analysis of the data, including the characterization of the host star, the derived properties of the planet, and the limits on any additional planets in the system. In Section 4 we compare TOI-257b with the demographics of the known exoplanets, and discuss the significance of the system. We provide concluding remarks and suggestions for future work in Section 5.

2 OBSERVATIONS AND DATA REDUCTION

TOI-257 (HD 19916) is a bright ($V = 7.570$ mag) late F-type star, located at a distance of 77.1 ± 0.2 pc (parallax of 12.9746 ± 0.0327 mas from *Gaia* DR2, Gaia Collaboration et al. 2018a). The star is slightly evolved with a radius of $1.888 \pm 0.033\,R_\odot$, mass of $1.390 \pm 0.046\,M_\odot$, and surface gravity of $\log g = 4.030 \pm 0.011$ dex, derived from the asteroseismic analysis of the *TESS* photometry in Section 3.2. The star has an effective temperature of 6075 ± 90 K and metallicity of [M/H] $= 0.19 \pm 0.10$ derived from the analysis of Minerva-Australis spectra in Section 3.1 as well as a rotational velocity of $v \sin i = 11.3 \pm 0.5$ km s^{-1} in Section 3.3. TOI-257 has rotational period of 8.072 ± 0.268 days based on analysis of the *TESS* photometry in Section 3.3.

2.1 *TESS* Photometry

The star TOI-257 (HD 19916, TIC 200723869 Stassun et al. 2019) was observed in Sectors 3 and 4 by Camera 3 of the *TESS* spacecraft in 2-minute cadence mode nearly continuously between 2018 September 22 and 2018 November 15. The photometric data were processed by the Science Processing Operations Center (SPOC) pipeline as described in Jenkins et al. (2016). Overall, three transits were detected with depth of ~ 1500 parts per million (ppm) and duration of ~ 6 hours. Two transits are detected in sector 3 (on BJD 2458386 and BJD 2458404), and one in sector 4 (on BJD 2458422). The transit at the beginning of sector 3 was observed during an experiment to improve the spacecraft pointing[2], and the transit in sector 4 was observed during the thermal ramp.

The *TESS* light curves were accessed from the NASA's Mikulski Archive for Space Telescopes (MAST). The light curves had been processed by the *TESS* team using two different techniques: Pre-search Data Conditioning (PDC, the usual way of light curve

[1] Data from the NASA Exoplanet Archive, 6th November 2019

[2] See the data release notes at https://archive.stsci.edu/missions/tess/doc/tess_drn/tess_sector_03_drn04_v02.pdf

Table 1. Stellar Parameters for TOI-257. **Notes.**–[†]Priors used in the EXOFASTv2 global fit. [⋆]Upper limit on the V-band extinction from Schegel Dust maps.

Parameter	Value	Source
R.A. (hh:mm:ss)	03:10:03.982	*Gaia* DR2
Decl. (dd:mm:ss)	-50:49:56.58	*Gaia* DR2
μ_α (mas yr^{-1})	97.912 ± 0.052	*Gaia* DR2
μ_δ (mas yr^{-1})	27.911 ± 0.082	*Gaia* DR2
Parallax (mas)	12.9746 ± 0.0327	*Gaia* DR2
A_V (mag)	0.0165 ($\leq$ 0.0506) [†,⋆]	Schegel Dust maps
Broadband Magnitudes:		
B_T (mag)	$8.293^{+0.020}_{-0.016}$	Tycho
V_T (mag)	$7.612^{+0.020}_{-0.011}$	Tycho
$TESS$ (mag)	7.012 ± 0.017	*TESS* TIC v6
J (mag)	6.504 ± 0.020	2MASS
H (mag)	6.325 ± 0.020	2MASS
K_s (mag)	6.256 ± 0.020	2MASS
$WISE1$ (mag)	6.209 ± 0.100	WISE
$WISE2$ (mag)	6.084 ± 0.033	WISE
$WISE3$ (mag)	$6.239^{+0.030}_{-0.015}$	WISE
$WISE4$ (mag)	$6.172^{+0.100}_{-0.048}$	WISE
$Gaia$ (mag)	$7.417^{+0.020}_{-0.000}$	*Gaia* DR2
$Gaia_{BP}$ (mag)	$7.730^{+0.020}_{-0.002}$	*Gaia* DR2
$Gaia_{RP}$ (mag)	$6.994^{+0.020}_{-0.002}$	*Gaia* DR2
Spectroscopic Properties derived from Minerva-Australis spectra:		
$T_{\rm eff}$ (K)	6075 ± 90 [†]	iSpec; this paper
log g (dex)	3.97 ± 0.10	iSpec; this paper
[M/H] (dex)	0.19 ± 0.10 [†]	iSpec; this paper
$R_\star$ ($R_\odot$)	1.926 ± 0.017	isochrones; this paper
$M_\star$ ($M_\odot$)	$1.389^{+0.056}_{-0.009}$	isochrones; this paper
$\rho_\star$ (g cm^{-3})	0.275 ± 0.011	isochrones; this paper
$L_\star$ ($L_\odot$)	4.527 ± 0.120	isochrones; this paper
Age (Gyr)	3.11 ± 0.46	isochrones; this paper
$v \sin i$ (km s^{-1})	11.3 ± 0.5	LSD; this paper

extraction and removal of systematics, see, Jenkins et al. 2016) and Simple Aperture Photometry (SAP, see, Twicken et al. 2010). These raw SAP and PDC light curves are shown in Figure 1, along with their detrended versions.

To detrend the PDC light curves, we removed all quality-flagged data (except for stray light flag 2048), clipped 5σ outliers, removed stellar and instrumental variability, normalized with the mean of the out-of-transit flux, and merged together Sectors 3 and 4. To remove the photometric variability, we used a Savitzky-Golay (SG) filter with a kernel width of 501 data points and a polynomial of order 2 over 3 iterations. During detrending, the planetary transits were masked and then detrended by dividing out the interpolated SG-filtered flux values from the out-of-transit data points. The SG detrending removed any longer-period stellar variability and systematics, and retained any features that occurred on timescales comparable or shorter than the duration of planetary transits (Kinemuchi et al. 2012; Jenkins et al. 2016).

Two transits were recovered using the PDC technique, one in Sector 3 and one in Sector 4. The transit at the beginning of Sector 3 was missed by the PDC procedure since it falls on the part of the light curve that was quality-flagged for manual exclusion during a spacecraft pointing improvement experiment. To recover this transit event, we performed the exact same detrending procedure on the SAP version of the light curve as on the PDC light curve, the only difference being that the manual exclusion (flag 128) data points were not removed. The resulting detrended SAP light curve was used for recovering the first transit observed by *TESS* in Sector 3 but excluded from the global fit analysis as systematics were not removable as seen in Figure 1.

To include the first transit from Sector 3 in the global fit analysis, we created a custom light curve following the procedures of Vanderburg et al. (2019) to obtain a cleaner light curve relatively free from systematics and stellar variability. We started by using a larger 4.5 pixel radius aperture to extract the Sector 3 photometry, which reduced the amplitude of the systematics observed in the early part of the light curve compared to the *TESS* pipeline's SAP light curve. We then removed systematics from a small segment of the light curve surrounding the first transit (2458383.7 $< t <$ 2458388.0) by decorrelating against the median background flux value from outside the aperture for each 2-minute image and the standard deviation of the Q1, Q2, and Q3 quaternions within each 2-minute exposure. We excluded points during the planet transit in our decorrelation to prevent the systematics correction from biasing or distorting the shape of the transit. Next, we simultaneously fit the low-frequency variability (which we modeled as a basis spline) with a transit model in a similar manner to Vanderburg et al. (2016a), except that we did not also simultaneously fit for the systematics and we introduced a discontinuity at BJD 24581385.95 where we switch from the custom light curve to the PDC light curve. The combination of our custom light curve and the PDC light curve are what we use in the final global fitting analysis with EXOFASTv2 (Eastman et al. 2013; Eastman 2017; Eastman et al. 2019). Figure 2 is the resulting 30 minute binned and phase folded custom light curve along with the PDC light curve and the individual transits color coded.

2.2 Direct Imaging Follow-up

If a target star has a close companion, the additional flux from the second source can cause photometric contamination, resulting in an underestimated planetary radius, or be the source of an astrophysical false positive. To rule out the presence of close companions, speckle imaging observations were taken of TOI-257 with the SOAR and Zorro instruments.

2.2.1 *SOAR Speckle Imaging*

TOI-257 was observed with SOAR speckle imaging (Tokovinin 2018) on 18 February 2019 UT, observing in a similar visible bandpass as *TESS*. The 5σ detection sensitivity and the speckle auto-correlation function from the SOAR observation are plotted in Figure 3. Further details of the observations are available in Ziegler et al. (2020). No nearby stars were detected within 3″ of TOI-257.

2.2.2 *Gemini-South High-Resolution Speckle Imaging using Zorro*

Direct imaging observations of TOI-257 was also carried out on 12 Sept. 2019 UT using the Zorro speckle instrument on Gemini-South[3]. Zorro simultaneously provides speckle imaging in two bands, 562 nm and 832 nm, with output data products including a reconstructed image, and robust limits on companion detections (Howell et al. 2011). Figure 4 shows our 562 nm result and reconstructed speckle image and we find that TOI-257 is indeed a single star with no companion brighter than about 6 magnitudes detected

[3] https://www.gemini.edu/sciops/instruments/alopeke-zorro/

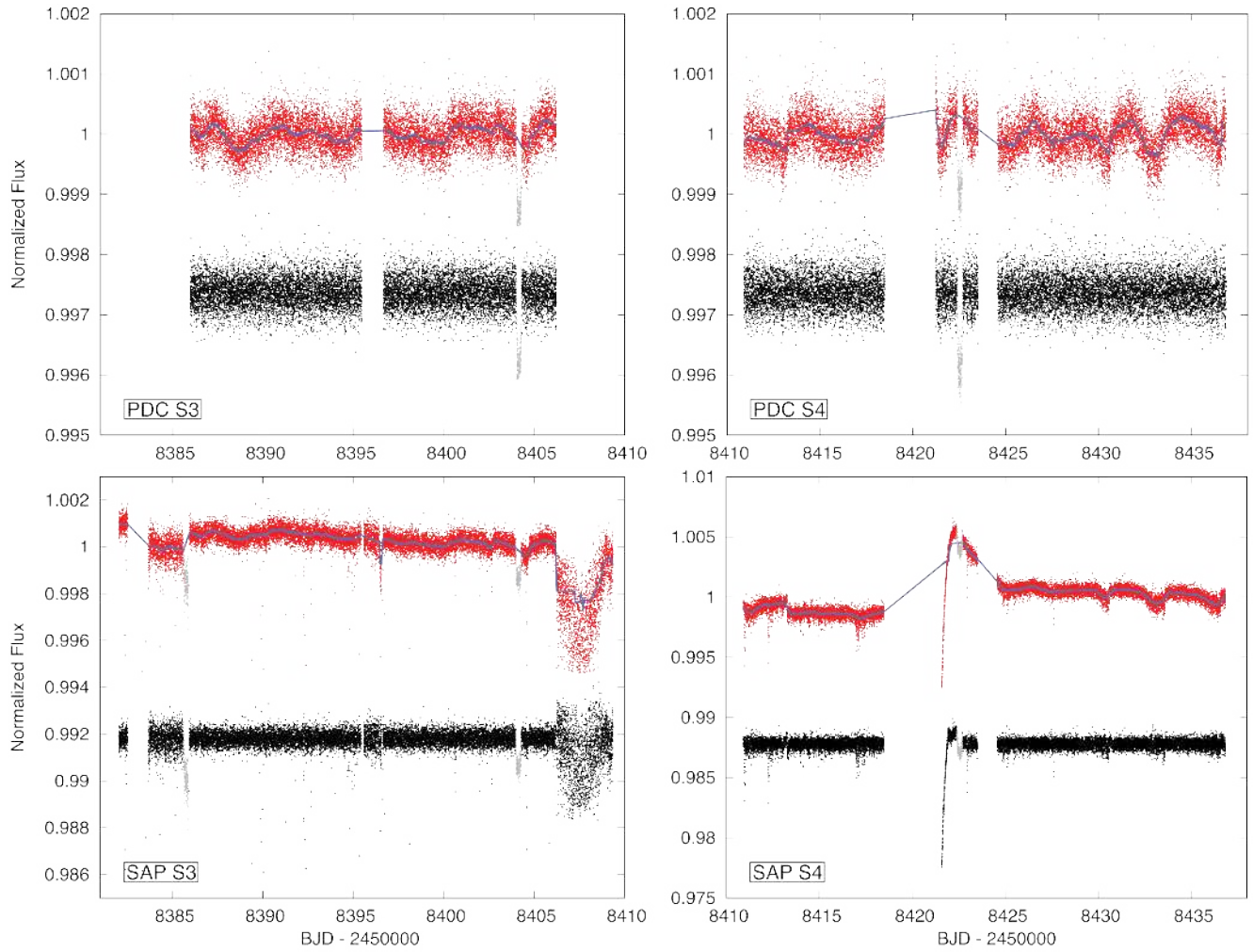

Figure 1. *TESS* light curves of TOI-257 from Sector 3 (left panel) and Sector 4 (right panel). The Pre-search Data Conditioning (PDC, upper panels) and Simple Aperture Photometry (SAP, lower panels) versions of the light curves before (shown in red) and after detrending (shown in black and shifted down arbitrarily to avoid overlap with the red points). The detrending function is blue and transits are grey. Top left: A single transit event was recovered by PDC in Sector 3. Top right: A single transit event was recovered by PDC in Sector 4. Bottom left: Two transit events were recovered by SAP from Sector 3. Bottom right: A single transit event was recovered by SAP in Sector 4.

within 1.75″. This limit corresponds to approximately an M3V star at the inner working angle of ~ 0.25″and M5V at the outer working angle of ~ 1.75″.

2.3 Spectroscopy

We obtained high-resolution spectroscopic observations of TOI-257 with Minerva-Australis, FEROS, and HARPS to confirm and measure the mass of the *TESS* transiting planet candidate. Here we describe the observations from each spectrograph and list the derived radial velocities in Table 2.

2.3.1 High-Resolution Spectroscopy with Minerva-*Australis*

We carried out an intensive radial velocity follow-up campaign with the Minerva-Australis facility to confirm the planetary nature of the transit-like signals in the *TESS* photometry, measure the mass and orbital properties of the planet, search for any additional planets in the system, and measure the stellar atmospheric properties of the host star. A total of 53 spectra (observations taken simultaneously from multiple telescopes in the array are counted as one observation) of TOI-257 were obtained at 28 epochs between 2019 July 12 and October 15. Telescopes T1, T3, T4, and T5 in the Minerva-Australis array simultaneously feed via 50 μm circular fiber cables a single KiwiSpec R4-100 high-resolution (R = 80,000) spectrograph (Barnes et al. 2012) with wavelength coverage from 500 to 630 nm.

Radial velocities are derived for each telescope using the least-squares technique of Anglada-Escudé & Butler (2012) and corrected for spectrograph drifts with simultaneous Thorium-Argon arc lamp observations. We observed TOI-257 with up to four telescopes simultaneously with one or two 20 to 30-minute exposures per epoch. The radial velocities from each telescope are given in Table 2 labeled by their fiber number. Each telescope (fiber) has its own velocity zero-point which is modeled as a free parameter, and the mean uncertainty of the Minerva-Australis observations is 7.6 m s^{-1}. The radial velocities collected by Minerva-Australis show a ~ 10 m s^{-1} sinusoidal variation that is in phase with the photometric ephemeris

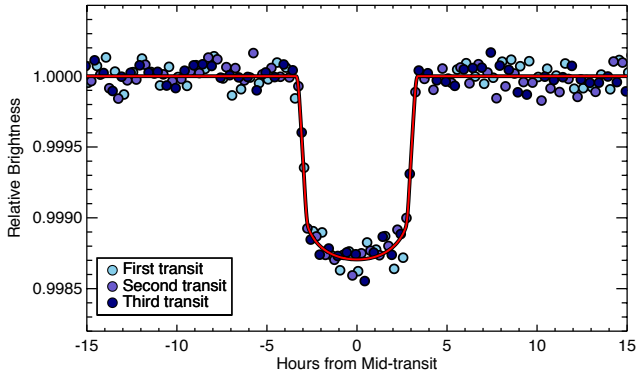

Figure 2. Phase folded *TESS* light curve of TOI-257 binned at a cadence of 30 minutes with the individual transits color coded showing that they are of similar depth. The first transit comes from the custom light curve where we removed systematics that are the result of a spacecraft pointing anomaly. The second and third transit are from the Pre-search Data Conditioning light curve. The red curve is the best-fit transit model.

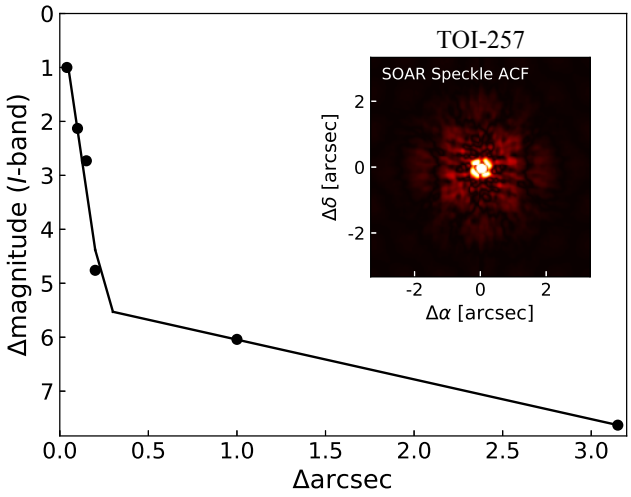

Figure 3. The 5σ detection sensitivity and inset speckle auto-correlation function from SOAR speckle observing of TOI-257 on 18 February 2019 UT in *I*-band, which is similar to the *TESS* bandpass. The orientation of the inset image has North pointed up and East to the left. No stars were detected within 3″ of TOI-257.

with an amplitude compatible with a sub-Saturn-sized planet in a moderately eccentric orbit as shown in Figures 9 and 10. Additionally, we measured the bisector velocity span (BVS) values using the cross-correlation functions (CCFs) as a check to ensure that the radial velocity variation observed is not from stellar activity or a background eclipsing binary system. As shown in Figure 11, no correlations are apparent in the BVS values.

2.3.2 *High-Resolution Spectroscopy with the Fiber-fed Extended Range Optical Spectrograph (FEROS)*

TOI-257 was observed with the FEROS instrument (R = 48,000, Kaufer et al. 1999) on the MPG 2.2 m telescope at La Silla Observatory between 15 December 2018 and 22 January 2019. We collected a total of eight spectra and the observations were performed in simultaneous calibration mode, utilizing the ThAr lamp on the secondary fiber to track and remove instrumental variations due to changes in the temperature and pressure during the science exposures. The exposure times were set to 300 s, resulting in signal-to-noise ratio between 270 and 370 per resolution element. We produced radial velocities by cross-correlation with a G2-type binary mask template using the CERES pipeline (Brahm et al. 2017), which also corrects the radial velocities for instrumental systematics and the Earth's motion.

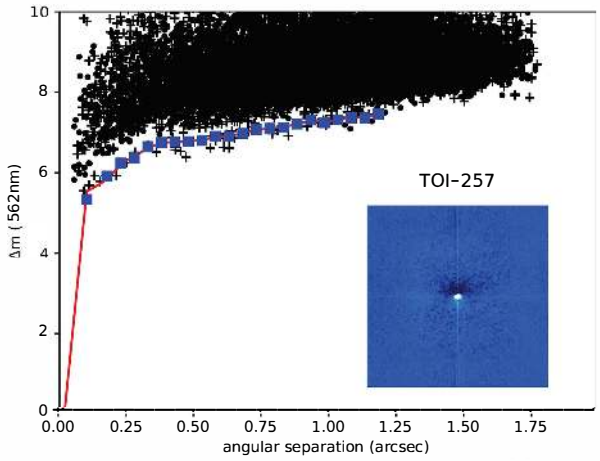

Figure 4. Zorro speckle observation of TOI-257 taken at 562 nm. Our simultaneous 832 nm observation provides a similar result. The red line fit and blue points represent the 5σ fit to the sky level (black points) revealing that no companion star is detected from the diffraction limit (17 mas) out to 1.75″within a Δ mag of 6 to 8.″across. The inset reconstructed speckle image has north up and East to the left and is 2.5″across.

2.3.3 *High-Resolution Spectroscopy with the High Accuracy Radial velocity Planet Searcher (HARPS)*

We monitored TOI-257 with the HARPS spectrograph (R = 120,000, Mayor et al. 2003) on the ESO 3.6 m telescope at La Silla Observatory between December 2018 and November 2019. A total of 33 observations were obtained and the data was processed using the HARPS data analysis pipeline (Queloz et al. 2009). The exposure times were set to 300 s, providing a signal-to-noise ratio between 90 and 180 per resolution element. We produced radial velocities by cross-correlation with a G2-type binary mask template.

3 ANALYSIS

3.1 Host Star Properties from Spectroscopy

We used the Minerva-Australis spectra to determine TOI-257's atmospheric stellar parameters. Through the python package iSpec (Blanco-Cuaresma et al. 2014; Blanco-Cuaresma 2019), we stacked the stellar spectra to derive the effective temperature, surface gravity, and overall metallicity ([M/H]) of the star. We configured the iSpec synthetic grid to incorporate a MARCS atmospheric model (Gustafsson et al. 2008) and utilized the spectrum (Gray & Corbally 1994) radiative transfer code. [M/H] was derived using version 5.0 of *Gaia*-ESO Survey's (GES) line-list (Heiter et al. 2015) normalized by solar values obtained by Asplund et al. (2009). Our synthetic spectra fit was constructed by setting initial values for $T_{\rm eff}$, log g and

Table 2. Journal of radial velocity observations of TOI-257. **Notes.**–M-A Tel3, M-A Tel4, and M-A Tel6 are MINERVA-Australis Telescope3, Telescope4, and Telescope6, respectively. (This table is available in its entirety in machine-readable form.)

Date (BJD)	RV ($m\,s^{-1}$)	σ ($m\,s^{-1}$)	Instrument
2458465.539980	21.9	2.0	HARPS
2458465.602650	26.7	2.0	HARPS
2458465.690670	26.1	2.0	HARPS
2458466.529660	24.8	2.0	HARPS
2458466.591590	17.1	2.0	HARPS
2458466.678080	23.5	2.0	HARPS
2458466.682320	22.5	2.0	HARPS
2458467.674470	12.5	5.3	FEROS
2458468.663190	8.1	5.5	FEROS
2458481.588670	20.9	2.0	HARPS
2458481.593290	24.6	2.0	HARPS
2458481.597630	24.1	2.0	HARPS
2458482.673800	32.1	2.0	HARPS
2458482.678140	29.7	2.0	HARPS
2458493.714430	-11.4	6.2	FEROS
2458497.608960	-10.3	5.7	FEROS
2458500.629830	-19.3	5.7	FEROS
2458505.566740	-14.6	5.9	FEROS
2458677.272975	10.8	3.0	M-A Tel3
2458677.272975	-13.2	3.4	M-A Tel4
2458677.294387	24.3	3.1	M-A Tel3
2458677.294387	10.3	3.4	M-A Tel4
2458680.203692	11.6	3.6	M-A Tel3
2458680.203692	20.7	4.1	M-A Tel4
2458680.203692	-8.2	7.5	M-A Tel5
2458680.225093	0.1	3.9	M-A Tel3
2458680.225093	3.3	3.8	M-A Tel4
2458680.225093	5.4	8.0	M-A Tel5
2458681.170185	1.9	3.5	M-A Tel3
2458681.170185	22.1	3.6	M-A Tel4
2458681.170185	-8.3	4.6	M-A Tel5
2458681.191597	-3.8	3.3	M-A Tel3
2458681.191597	-11.9	3.9	M-A Tel4
2458681.191597	14.9	4.6	M-A Tel5
2458682.146655	25.4	3.9	M-A Tel3
2458682.146655	27.6	7.2	M-A Tel4
2458682.146655	12.7	5.3	M-A Tel5
2458682.168067	14.9	3.9	M-A Tel3
2458682.168067	19.6	4.6	M-A Tel4
2458682.168067	5.0	5.6	M-A Tel5
2458683.249780	6.3	3.5	M-A Tel4
2458683.276111	-5.9	4.6	M-A Tel3

[M/H] of 6050 K, 4.44 dex, and 0.00 dex, respectively, based on the parameters from a broadband spectral energy distribution (SED) analysis. Figure 5 depicts our observed spectra and synthetic model produced by iSPEC. Our derived $T_{\rm eff}$, log g and [M/H] values were then fed into the Bayesian isochrone modeler ISOCHRONES (Morton 2015; Montet et al. 2015).

ISOCHRONES uses nested sampling scheme called MULTINEST (Feroz et al. 2009) to determine the stellar mass, radius, and age, which was then used to derive the stellar density and luminosity of TOI-257. For this particular analysis, we used the stellar parameter results from iSPEC as well as the parallax value from *Gaia* DR2 with G, H, J, K, V and W1 magnitudes as priors in the global fit. The spectroscopic stellar iSPEC and ISOCHRONES values can be found in Table 1 and are in good agreement with the SED analysis performed using `EXOFASTv2` and the asteroseismology. We then incorporated

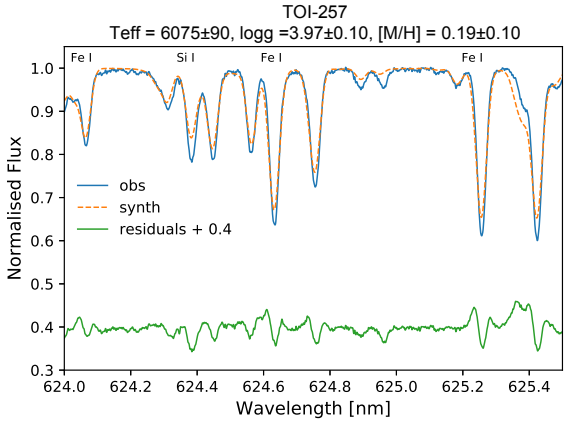

Figure 5. The best fit synthetic model spectrum from iSPEC (the red dashed line) of TOI-257 to that of the combined stellar spectrum obtained from the MINERVA-Australis spectroscopic observations (the blue solid line) for the wavelength region between 624.0 nm and 625.5 nm. The residuals of the fit are shown as the green solid line.

the $T_{\rm eff}$and [M/H] values derived from the iSPEC analysis of the MINERVA-Australis spectra as priors in the final `EXOFASTv2` global fit of the data in Section 3.4.

3.2 Asteroseismology

3.2.1 Global Asteroseismic Parameters

To perform asteroseismic analysis on TOI-257 we produced a custom light curve using the *TESS* Asteroseismic Science Operations Center (TASOC, Lund et al. 2017) photometry pipeline[4] (Handberg et al., in prep.), which is based on software originally developed to generate light curves for data collected by the K2 Mission (Lund et al. 2015). The TASOC pipeline implements a series of corrections to optimize light curves for an asteroseismic analysis (Handberg & Lund 2014), including the removal of instrumental artefacts and of the transit events using a combination of filters utilizing the estimated planetary period. The photometric performance of the TASOC light curve was comparable to the light curve produced by the SPOC pipeline.

Solar-like oscillations are broadly described by a frequency of maximum oscillation power ($\nu_{\rm max}$) and a large frequency separation ($\Delta\nu$), which approximately scale with log g and the mean stellar density, respectively (see, García & Ballot 2019). The power spectrum of the sector 3 light curve of TOI-257 displays a power excess near $\sim 1200\,\mu$Hz (Figure 6), consistent with the spectroscopic log g and the expected frequency range from the *TESS* asteroseismic target list (ATL, Schofield et al. 2019). An autocorrelation of the power spectrum reveals a peak at a frequency spacing consistent with the location of the excess power (e.g. Stello et al. 2009). Furthermore, the amplitude of the power excess (~ 9 ppm) is consistent with the expected value from observations by *Kepler* (Huber et al. 2011). The addition of the Sector 4 light curve reduced the significance of the asteroseismic detection due to the slightly elevated noise level, and was thus discarded for the remainder of our analysis.

To test the significance of the detection and measure $\nu_{\rm max}$ and $\Delta\nu$ we used 15 independent analysis methods within working

[4] https://tasoc.dk/code/

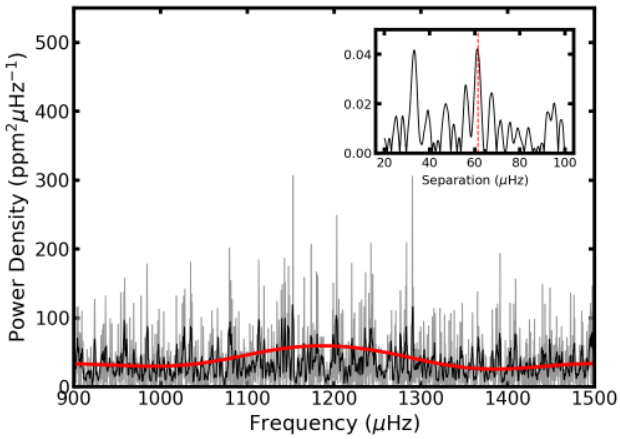

Figure 6. Power spectrum of the Sector 3 TASOC light curve of TOI-257 (grey line). The black and red lines show the power spectrum smoothed with a boxcar width of 2μHz and Gaussian with a full width at half max of $\Delta\nu$, respectively. The inset shows the autocorrelation of the power spectrum, with a red line marking the expected value of $\Delta\nu$ based on the location of the power excess.

group 1 of the *TESS* Asteroseismic Science Consortium (e.g. Huber et al. 2009; Mathur et al. 2010; Mosser et al. 2012; Benomar et al. 2012; Kallinger et al. 2012; Corsaro & De Ridder 2014; Davies & Miglio 2016; Campante 2018). All but one pipeline reported a significant detection of solar-like oscillations. The final parameters are $\nu_{\rm max} = 1188 \pm 40 \mu$Hz and $\Delta\nu = 61.4 \pm 1.5 \mu$Hz, with the central value taken from the solution closest to the median of all solutions, and uncertainties calculated from the median formal uncertainty returned by individual pipelines added in quadrature to the scatter over individual methods.

3.2.2 *Grid-Based Modeling*

We used a number of independent approaches to model the observed global asteroseismic parameters, including different stellar evolution codes (ASTEC, GARSTEC, MESA, and YREC, Christensen-Dalsgaard 2008; Weiss et al. 2008; Paxton et al. 2011, 2013, 2015; Choi et al. 2016a; Demarque et al. 2008) and modeling methods (BeSPP, BASTA, PARAM, isoclassify, Silva Aguirre et al. 2015; Serenelli et al. 2017; Rodrigues et al. 2014, 2017; Huber et al. 2017; García Saravia Ortiz de Montellano et al. 2018). Model inputs included the spectroscopic temperature and metallicity (see Section 3.1), $\nu_{\rm max}$, $\Delta\nu$, and the luminosity derived from the Gaia parallax. To investigate the effects of different input parameters, modelers were asked to provide solutions with and without taking into account the luminosity constraint.

The modeling results showed a bi-modality in mass (and thus age) at $\sim 1.2\,M_\odot$ and $\sim 1.4\,M_\odot$, with all pipelines favoring the higher mass solution once the luminosity constraint was included. We adopted the solution closest to the median of all returned values, with uncertainties calculated by adding the median uncertainty for a given stellar parameter in quadrature to the standard deviation of the parameter for all methods. This method has been commonly adopted for *Kepler* (e.g. Chaplin et al. 2014) and captures both random and systematic errors estimated from the spread among different methods. The final estimates of stellar parameters are summarized in Table 3.2.2, constraining the radius, mass, density and age of TOI-257 to ~ 2 %, ~ 3 %, ~ 3 % and ~ 13 %. We emphasize that these uncertainties in stellar parameters are robust against systematic errors from different stellar model grids, which are frequently neglected when characterizing exoplanets. The stellar mass and radius derived from this analysis is used as priors in the final `EXOFASTv2` global fit of the data in Section 3.4.

Table 3. Asteroseismic Stellar Parameters for TOI-257. **Notes:** †Priors used in the `EXOFASTv2` global fit.

Input Parameters	
Frequency of maximum oscillation power, $\nu_{\rm max}$ (μHz),	1188 ± 40
Large frequency separation, $\Delta\nu$ (μHz),	61.4 ± 1.5
Effective Temperature, $T_{\rm eff}$ (K)	6075 ± 90
Metallicity, [Fe/H] (dex)	0.19 ± 0.10
Luminosity, L ($L_\odot$)	4.57 ± 0.16
Stellar Parameters	
Stellar Mass, $M_\star$ ($M_\odot$)	1.390 ± 0.046 †
Stellar Radius, $R_\star$ ($R_\odot$)	1.888 ± 0.033 †
Stellar Density, $\rho_\star$ (cgs)	0.293 ± 0.011
Surface Gravity, $\log g$ (cgs)	4.030 ± 0.011
Age, t (Gyr)	3.46 ± 0.43

3.3 Stellar Rotation Period Estimates

The rotation period of TOI-257 was estimated by performing Lomb-Scargle (Scargle 1982) periodogram and auto-correlation function analysis (e.g., McQuillan et al. 2013) on the *TESS* lightcurve, and by measuring the projected stellar rotation velocity ($v \sin i$) from Minerva-Australis spectra.

We calculated the Lomb-Scargle periodograms for the raw *TESS* light curves from Sectors 3 and 4 individually and from the combined light curve of the two Sectors, after masking the transit events. For Sector 3, the periodogram shows that the variability has a period of $P = 5.01 \pm 0.46$ days and amplitude of $A = 114 \pm 2$ ppm. Sector 4 light curve has a variability with a period of $P = 4.13 \pm 0.22$ days and amplitude of $A = 144 \pm 2$ ppm. The period and amplitude from the two Sectors is reasonably consistent. Performing this analysis on the combined light curves reveals that the variability has a period of $P = 4.04 \pm 0.13$ d, amplitude of $A = 88 \pm 1$ ppm, and false alarm probability (FAP)<< 0.01. A second very strong peak is observed at ~ 2.69 days (or $2P/3$) in the Lomb-Scargle periodograms. The FAP was computed from Monte Carlo simulations (e.g., Messina et al. 2010) and the uncertainty in the period of variability was calculated following the procedure of Lamm et al. (2004). The variability from both sectors combined phases-up well at a period of 4.036 days as shown in Figure 7, which indicates that the variability is likely to be astrophysical in nature (from stellar rotation and star spots) and not systematics. We therefore have adopted the period of variability as 4.04 ± 0.13 d.

We also performed an auto-correlation function analysis on the light curves from the individual sectors and combined sectors, and find that the period of variability as $P = 5.03 \pm 0.61$ days and $P = 4.12 \pm 0.32$ days for Sectors 3 and 4, respectively, and a period of $P = 4.14 \pm 0.22$ days for the combined light curves. We also find a strong secondary period in the combined light curves of ~ 2.7 days. These results are consistent with the periods found from the Lomb-Scargle periodograms.

To determine whether the period of variability is the true rotation period of the star or one of its harmonics, we calculate an

upper limit on the rotation period from the star's $v \sin i$ and estimated radius. We measured the $v \sin i$ of TOI-257 by fitting a rotationally broadened Gaussian (Gray 2005) to a least-squares deconvolution profile (Donati & Collier Cameron 1997) obtained from the sum of all the spectral orders from the combined highest S/N spectra of TOI-257. The resulting $v \sin i$ is 11.3 ± 0.5 km s^{-1} and combined with the stellar radius from asteroseismology of $R_\star = 1.89 \pm 0.33$ $R_\odot$, sets the upper limit on the rotation period for the star of ~ 8.5 days, assuming that the inclination of the stellar rotation axis is near 90 deg to the line of sight.

Given the above analyses, we attribute the 4.04 day period of variability observed in the combined *TESS* light curve to be half the true rotation period of 8.08 ± 0.26 days (which gives a $v_{rot} = 2 * \pi * R_\star / P_{rot} = 11.8$ km s^{-1}, consistent with the value of $v \sin i$). The very strong secondary peak observed at ~ 2.7 days in both the Lomb-Scargle periodograms and the auto-correlation function analysis provides further evidence in support of the 8.08 ± 0.26 days being the true rotation period since the secondary peak corresponds nicely with the $P_{rot}/3$ harmonic. It is common for the observed rotational modulation to be at one or more of the harmonics, in particular at half and one-third the true rotation period (Vanderburg et al. 2016b). If the rotation period is 4.04 days, we would have expected to find a strong secondary peak at ~ 2.02 days instead of ~ 2.7 days. Given that the rotational period and stellar radius gives a rotational velocity consistent with the measured $v \sin i$, this suggest that the stellar obliquity is low (i.e., $i_\star \sim 90$ deg).

3.4 Planetary System Parameters from Global Analysis

To determine the system parameters for TOI-257 and its planet, we used `EXOFASTv2` (Eastman et al. 2013; Eastman 2017; Eastman et al. 2019) to perform a joint analysis of the *TESS* photometry and the radial velocity data. We placed Gaussian priors on $T_{\rm eff}$ and [Fe/H] from the Minerva-Australis high-resolution spectroscopy and Gaussian priors on R_* and M_* from asteroseismology. We applied an upper limit on the V-band extinction from the Schlafly & Finkbeiner (2011) dust maps at the location of TOI-257. We also performed a separate SED analysis (so as not to double count information used from the asteroseismic priors) as an independent check on the stellar parameters using catalog photometry from Tycho (Høg et al. 2000), 2MASS (Cutri et al. 2003), WISE (Cutri & et al. 2013), and *Gaia* (Gaia Collaboration et al. 2018b) as well as MIST stellar evolutionary models (Dotter 2016; Choi et al. 2016b). Gaussian priors were placed on the parallax from *Gaia* DR2, adding 82 μas to correct for the systematic offset found by Stassun & Torres (2018) and adding the 33 μas uncertainty in their offset in quadrature to the *Gaia*-reported uncertainty. Table 1 lists the broadband magnitudes used in the SED analysis and the stellar parameters including the ones used as priors in the global analysis.

The resulting best-fit models for the transit light curves are plotted in Figure 8, and for the radial velocities in Figures 9 and 10. A summary of the best-fit model values is given in Table 4. Figure 11 is a plot of the bisector velocity span showing no correlation between the bisectors and the radial velocities for the Minerva-Australis observations, indicating that the measured radial velocity signal is likely planetary in nature and not due to stellar photospheric activity (Figueira et al. 2013).

From the best-fit Kurucz stellar atmosphere model from the SED and the best-fitting MIST stellar evolutionary model, we find that TOI-257 is a somewhat evolved late-F star with $R_* = 1.951^{+0.066}_{-0.051}$ $R_\odot$, $M_* = 1.35^{+0.12}_{-0.38}$ $M_\odot$, $T_{\rm eff} = 6066^{+86}_{-110}$ K, and $\log g = 3.986^{+0.047}_{-0.150}$ (where g is in units of cm s^{-2}). These stellar parameters are in reasonably good agreement with the parameters derived from the Minerva-Australis spectroscopy and asteroseismology. However, we choose not to adopt these stellar parameters since they are not as precise as the ones derived from spectroscopy and asteroseismology and list the stellar parameters derived from the joint analysis of the *TESS* photometry and the radial velocity data in Table 4. From the joint analysis, we find that TOI-257 hosts a sub-Saturn sized planet with a radius of $R_P = 0.626^{+0.013}_{-0.012}$ R$_{\rm J}$ ($7.02^{+0.15}_{-0.13}$ $R_\oplus$) and mass of $M_P = 0.134^{+0.023}_{-0.022}$ M$_{\rm J}$ ($42.6^{+7.3}_{-7.0}$ $M_\oplus$), on a moderately eccentric ($e = 0.242^{+0.040}_{-0.065}$) ~ 18.4 day orbit.

3.5 Complementary Analysis, and Limits on Additional Planets

We further analyze the radial velocity data set in Table 2 with `RadVel` (Fulton et al. 2018) to provide both an independent analysis for checking consistency in the mass and eccentricity of planet b, and to search for any additional planets. The search for additional planets is motivated by two reasons. First, moderately eccentric Keplerian signals can sometimes resolve into two near-circular resonant signals with additional radial velocity data (e.g. Wittenmyer et al. 2013; Trifonov et al. 2017; Boisvert et al. 2018; Wittenmyer et al. 2019). Second, we wish to evaluate the multiplicity of systems like TOI-257 with warm sub-Saturns.

To apply `RadVel`, we first median subtract and average the Minerva-Australis radial velocities from individual telescopes across nights, weighted by the error bars of each measurement. The radial velocity data sets are assumed to be independent in `RadVel` for the statistical assessment of models. By binning the data across Minerva-Australis telescopes, we avoid needing to account for the systematics common to all three Minerva-Australis radial velocities.

The combined analysis of the HARPS, binned Minerva-Australis, and FEROS data sets are consistent with a planet at the known transiting period and T_c from Table 4. However, the circular orbital solution is marginally favored over an eccentric model, according to the relative small-sample Akaike Information Criterion (ΔAICc=4.67) (Akaike 1974; Burnham & Anderson 2002). We fix P and T_c to the values independently derived from the `ExoFASTv2` analysis of the *TESS* light curve as they will not be well-constrained from the RVs alone, considering the small baseline compared to the orbital period. Since we do not jointly model the light curve with the radial velocities in `RadVel`, we are not capturing the additional information from the transit duration (~ 7.804 hr for circular orbit versus the measured 6.346 hr measured) and shape present in the light curve that may contribute to the increased evidence for an eccentric orbital solution presented earlier with `ExoFASTv2`. The best fit semi-amplitude from `RadVel` is similar to the `EXOFASTv2` results when using the unbinned Minerva-Australis radial velocities (9.2 ± 1.3 m s^{-1}); however the eccentric model is still not exclusively favored over a circular model (ΔAICc=3.97).

The remaining scatter after removing planet b is consistently larger than the uncertainties of the three instruments and appears structured (see Figure 12). We use a custom modified version of `RadVel` to generate log-likelihood periodograms (LLPs) with various orbit assumptions to search for additional planets. We start with a single planet model and generate a log-likelihood for a wide range in fixed periods, fitting only for T_c and K, as well as the relative instrument dependent offsets and additional radial velocity "jitter" noise terms, and then a second LLP assuming a fixed period and

Table 4. Median values and 68% confidence interval for TOI-257 from the MCMC `EXOFASTv2` analysis. **Notes.** – M-A T3, M-A T4, and M-A T6 are MINERVA-Australis Telescope3, Telescope4, and Telescope6, respectively. *The time of conjunction that is closest to the starting value supplied as a prior and is typically a good approximation for the mid transit time. ◇The optimal conjunction time is the time of conjunction that minimizes the covariance with the orbital period and therefore has the smallest uncertainty. ^The equilibrium temperature of the planet assumes no albedo and perfect heat redistribution. ⋆The tidal circularization timescale is calculated using Equation 3 from Adams & Laughlin (2006) and assuming a $Q = 10^6$. †*TESS* LC1 is the *TESS* light curve from PDC and *TESS* LC2 is the *TESS* light curve produced using the Vanderburg et al. (2019) procedures.

Parameter	Description	Values				
Stellar Parameters:						
M_*	Mass ($M_\odot$)	1.394 ± 0.046				
R_*	Radius ($R_\odot$)	1.883 ± 0.033				
L_*	Luminosity ($L_\odot$)	$4.41^{+0.31}_{-0.29}$				
ρ_*	Density (cgs)	$0.294^{+0.019}_{-0.017}$				
$\log g$	Surface gravity (cgs)	4.032 ± 0.021				
$T_{\rm eff}$	Effective Temperature (K)	6096 ± 89				
[Fe/H]	Metallicity (dex)	0.177 ± 0.099				
Planetary Parameters:		b				
P	Period (days)	18.38827 ± 0.00072				
R_P	Radius ($R_{\rm J}$)	$0.626^{+0.013}_{-0.012}$				
M_P	Mass ($M_{\rm J}$)	$0.134^{+0.023}_{-0.022}$				
T_C	Time of conjunction ($\rm BJD_{TDB}$)	$2458385.7600 \pm 0.0011^*$				
T_0	Optimal conjunction Time ($\rm BJD_{TDB}$)	$2458404.14831 \pm 0.00056^\diamond$				
a	Semi-major axis (AU)	0.1523 ± 0.0017				
i	Inclination (Degrees)	$88.78^{+0.78}_{-0.57}$				
e	Eccentricity	$0.242^{+0.040}_{-0.065}$				
ω_*	Argument of Periastron (Degrees)	96 ± 22				
T_{eq}	Equilibrium temperature (K)	1033^{+19}_{-18} ^				
$\tau_{\rm circ}$	Tidal circularization timescale (Gyr)	1880^{+400}_{-360} ⋆				
K	RV semi-amplitude (m/s)	8.5 ± 1.4				
R_P/R_*	Radius of planet in stellar radii	$0.03414^{+0.00037}_{-0.00029}$				
a/R_*	Semi-major axis in stellar radii	$17.39^{+0.36}_{-0.35}$				
δ	Transit depth (fraction)	$0.001166^{+0.000025}_{-0.000020}$				
τ	Ingress/egress transit duration (days)	$0.00947^{+0.0016}_{-0.00072}$				
T_{14}	Total transit duration (days)	$0.2644^{+0.0017}_{-0.0013}$				
T_{FWHM}	FWHM transit duration (days)	0.2548 ± 0.0010				
b	Transit Impact parameter	$0.28^{+0.17}_{-0.19}$				
ρ_P	Density (cgs)	$0.67^{+0.13}_{-0.12}$				
$logg_P$	Surface gravity	$2.927^{+0.072}_{-0.081}$				
Θ	Safronov Number	$0.0467^{+0.0080}_{-0.0078}$				
$\langle F \rangle$	Incident Flux (10^9 erg s^{-1} cm^{-2})	$0.245^{+0.018}_{-0.017}$				
T_P	Time of Periastron ($\rm BJD_{TDB}$)	$2458367.59^{+0.68}_{-0.69}$				
T_A	Time of Ascending Node ($\rm BJD_{TDB}$)	$2458382.34^{+0.43}_{-0.54}$				
T_D	Time of Descending Node ($\rm BJD_{TDB}$)	$2458370.58^{+0.48}_{-0.40}$				
$e\cos\omega_*$		$-0.026^{+0.083}_{-0.084}$				
$e\sin\omega_*$		$0.225^{+0.040}_{-0.068}$				
M_P/M_*	Mass ratio	$0.000092^{+0.000016}_{-0.000015}$				
d/R_*	Separation at mid transit	$13.42^{+1.2}_{-0.88}$				
Wavelength Parameters:		*TESS*				
u_1	linear limb-darkening coeff	0.222 ± 0.031				
u_2	quadratic limb-darkening coeff	0.274 ± 0.034				
A_D	Dilution from neighboring stars	≤ 0.00053				
Telescope Parameters:		FEROS	HARPS	M-A T3	M-A T4	M-A T6
$\gamma_{\rm rel}$	Relative RV Offset (m/s)	-5.6 ± 5.3	28.7 ± 1.5	1.0 ± 2.0	0.1 ± 2.0	-0.8 ± 2.1
σ_J	RV Jitter (m/s)	$13.3^{+6.9}_{-4.3}$	$7.07^{+1.2}_{-0.94}$	$13.9^{+1.7}_{-1.4}$	$14.0^{+1.7}_{-1.4}$	$13.9^{+1.8}_{-1.5}$
σ_J^2	RV Jitter Variance	175^{+230}_{-95}	49^{+18}_{-12}	194^{+49}_{-37}	197^{+50}_{-38}	193^{+53}_{-40}
Transit Parameters:		*TESS* LC1†	*TESS* LC2†			
σ^2	Added Variance	$1.70 \pm 0.12 \times 10^{-8}$	$1.33^{+0.60}_{-0.56} \times 10^{-8}$			
F_0	Baseline flux	1.0000009 ± 0.0000034	1.000001 ± 0.000010			

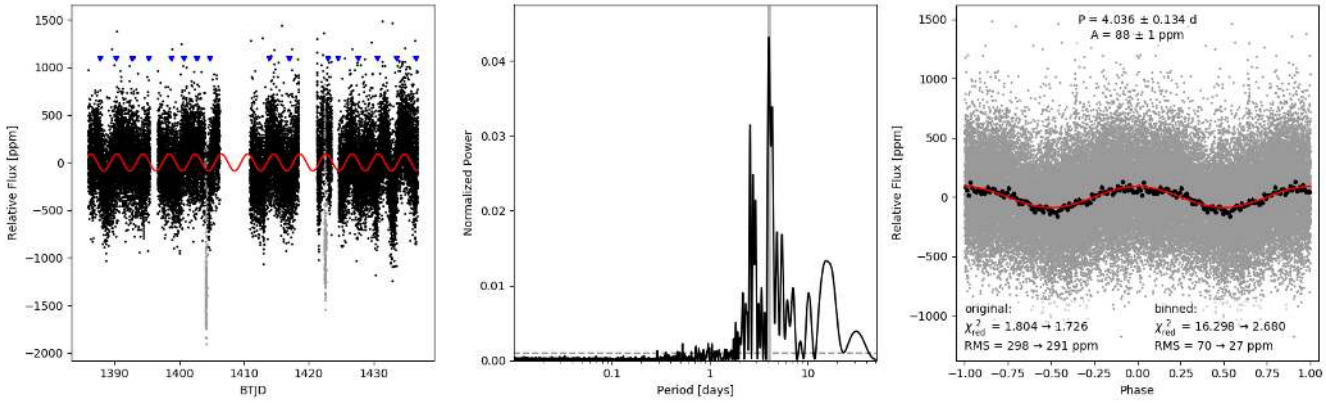

Figure 7. The left panel shows the *TESS* light curve of TOI-257 from Sectors 3 and 4 with the best-fit variability. The middle panel is the Lomb-Scargle periodogram for raw light curves from Sectors 3 and 4 combined. The right panel is the phase-folded light curve at the peak period found from the Lomb-Scargle periodogram.

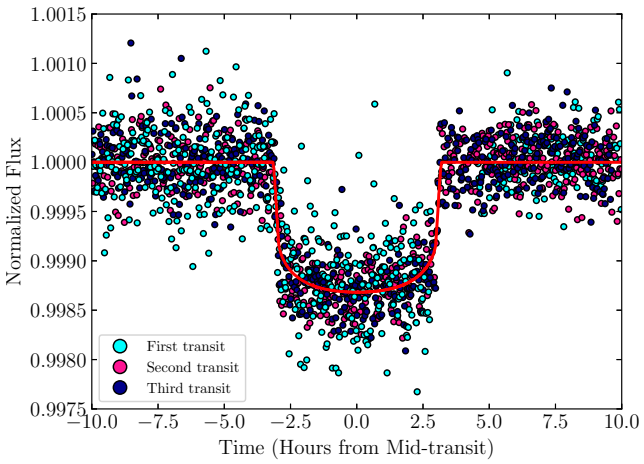

Figure 8. Phase folded *TESS* light curve of TOI-257 with the individual transits color coded similar to Figure 2. The red solid line is the best-fitting model.

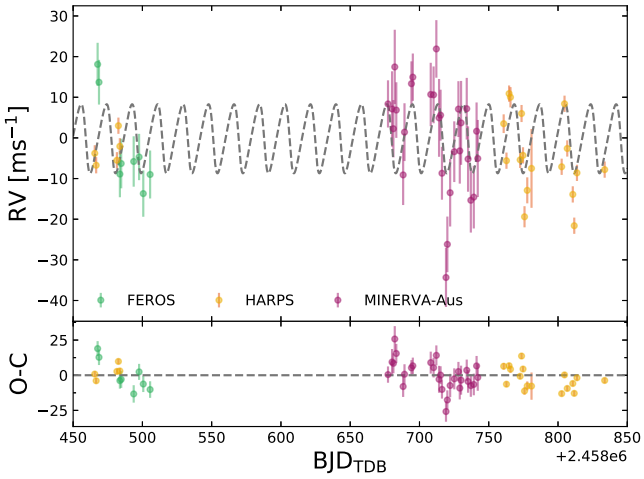

Figure 9. Radial velocity measurements of TOI-257 as a function of time. The radial velocity measurements from each instrument have been binned by day for clarity, however, the analysis was performed using the unbinned data. MINERVA-Australis radial velocities are represented by the purple filled-in circles. Radial velocities from FEROS and HARPS are the lime green and gold filled-in circles, respectively. The best-fit model is plotted as the dashed grey line and the center-of-mass velocity has been subtracted. The bottom panel shows the residuals between the data and the best-fit model.

T_c for planet b, but varying both semi-amplitudes to search for an additional planet candidate TOI-257c. Anecdotally, we observe that allowing for eccentric orbits in LLPs typically results in a noisier LLP compared to considering only circular orbits, and can particularly yield false peaks where $e \approx 1$ with the region of largest $|dRV/dt|$ located where the radial velocities are minimally sampled. These are likely non-physical orbits, so we only present circular searches (similarly, considering only eccentricities $\lesssim 0.5$ mitigates this effect).

Both the single planet model LLP and the two planet model LLP feature a peak near 71 days (Fig. 14). Including a circular planet near the 71 day peak, with no prior on T_c, yields a posterior probability distribution of the semi-amplitude for the second planet that is $> 4\sigma$ deviant from 0, and minimally affects the statistical significance of the first planet (as shown in Figure 13). The model comparison heavily favors the 2-planet model over the 1-planet model with ΔAICc = 23.67. This 71 day signal translates to approximately a 0.2% transit depth assuming the mass-radius relation given by Chen & Kipping (2017) and stellar parameters in Table 4. Figures A1 and A2 in the Appendix shows the posterior distributions from `RadVel` for a 1-planet and 2-planet circular models, respectively. We see no evidence for a transit in the *TESS* light curve within the uncertainty window of the best fit T_c for the possible outer planet. While this radial velocity detection is significant, more high-precision radial velocity measurements are needed to ensure the candidate c planet signal is not an alias or possible a result of the observing cadence, especially without an observed transit event.

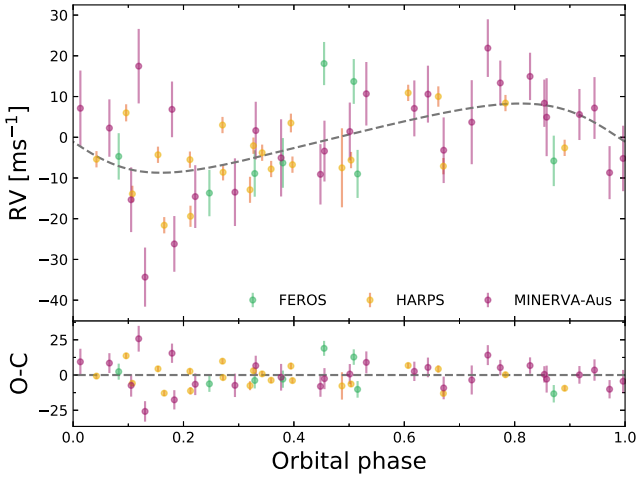

Figure 10. Same as Figure 9 but phased to one orbital period. The units of the horizontal axis were chosen so that the transit mid-time corresponds to an orbital phase of 0.25.

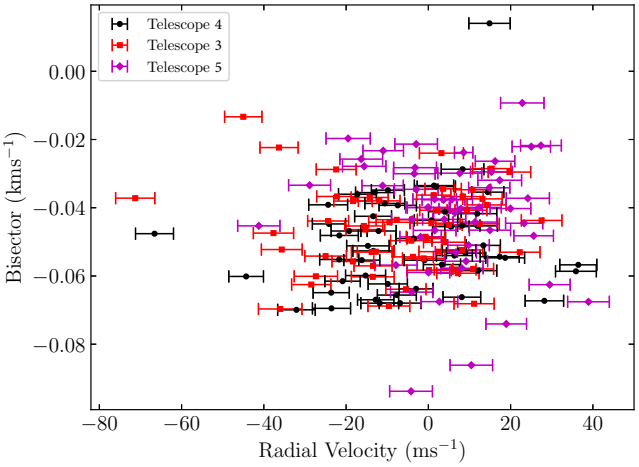

Figure 11. Bisector velocity span as a function of the radial velocities for the MINERVA-Australis radial velocities. There is no significant correlation between the bisector velocity span and the radial velocities.

3.6 Assessing the Level of Stellar Activity Present in the Radial Velocities

Next, we consider the possibility that the excess radial velocity residuals after modeling planet b are due to stellar activity rather than a second planet (or both) as presented in the previous subsection. `EXOFASTv2` does not permit the inclusion of a stellar activity model for the radial velocities, whereas `RadVel` does. With our customized version of `RadVel`, we calculate LLPs using a Gaussian Process (GP) with a quasi-periodic kernel (Rajpaul et al. 2015)[5] to approximate any detectable stellar-activity. We re-run the MCMC analysis for 1- and 2-planet models. We assume broad Gaussian priors on the GP hyper-parameters listed in Table 5. Both ~4 or 8 day

[5] The specific implementation of the quasi-periodic kernel in `RadVel` can be found on `https://radvel.readthedocs.io/en/latest/tutorials/GaussianProcess-tutorial.html`

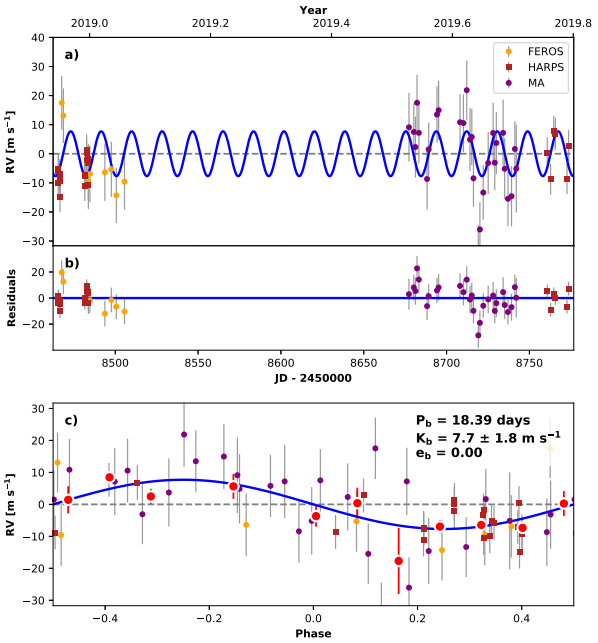

Figure 12. a) Best-fit 1-planet Keplerian orbital model for TOI-257. The maximum likelihood model is plotted in blue. We add in quadrature the radial velocity jitter terms listed in Table 4 with the measurement uncertainties for all radial velocities to determine individual error bars. **b)** Residuals to the best fit 1-planet model. **c)** Radial velocities phase-folded to the period of planet b. Red circles are the individual velocities binned in 0.08 units of orbital phase.

GP period produce qualitatively similar LLPs and mitigate peaks less than the candidate $P_{\rm rot}$ and show strong evidence for both the transiting planet and the candidate planet near 71 days (Figure 14). However, the evidence for a GP to model the remaining scatter is minimal. Both 1- and 2-planet models favor a single per-instrument Gaussian noise model over a 4 day GP (ΔAICc=3.22), while the GP is only marginally favored for the 8 day period case (ΔAICc=0.72). However, a 2-planet model with a GP is still favored over the corresponding 1-planet model (ΔAICc=6.34). Figures A3 and A4 in the Appendix shows the posterior distributions from `RadVel` with a quasi-periodic Gaussian Process for a 1-planet and 2-planet circular models, respectively.

Despite being statistically favored ($\sim 5.1\sigma$ detection), we do not claim TOI-257c as a confirmed planet, and relegate it to a "statistically validated" candidate status. Nava et al. (2019) has shown that activity can introduce spurious periodogram peaks at orbital periods longer than the stellar rotation period over the course of a single season, particularly for radial velocities that are unevenly sampled as is the case herein, notably for the HARPS data. However, with adequately sampled data (densely sampled with nightly cadence), Vanderburg et al. (2016b) find no evidence of spurious radial velocity periodogram peaks at periods longer than the stellar rotation period. As such, additional radial velocity monitoring over future seasons or novel stellar-activity mitigation approaches will be necessary to confirm the candidate second planet signal at ~71 days. Lastly, with no evidence for transits elsewhere in the light-curve, we can attribute the significant LLP peaks interior to planet b as a result of stellar-activity and/or a nightly observing cadence.

Table 5. Gaussian and min/max priors for quasi-periodic hyper-parameters for TOI-257 used in `RadVel`. **Notes.**–(a) These interpretations are further subject to the specific combination of values for the hyper-parameters, notably for cases with significantly different length and timescale factors. See Angus et al. (2018) for further discussion. (b) Also used for the initial guess.

Parameter	Unit; Physical Interpretation[a]	μ^b	σ	Min	Max	Citation
η_1	m s^{-1}, RV amplitude	10	None	0	100	stddev. of RVs, over-estimate
η_2	days, star-spot decay time-scale	10	5	0	100	Estimated from Giles et al. (2017), Fig. 5
η_3	days, quasi-period	4.036 ($\times$ 2)	0.134 ($\times$ 2)	0	100	*TESS* light curve; Section 3.3, this paper
η_4	none, period length scale	0.3525	0.044	0	100	Dai et al. (2017); Haywood et al. (2018)

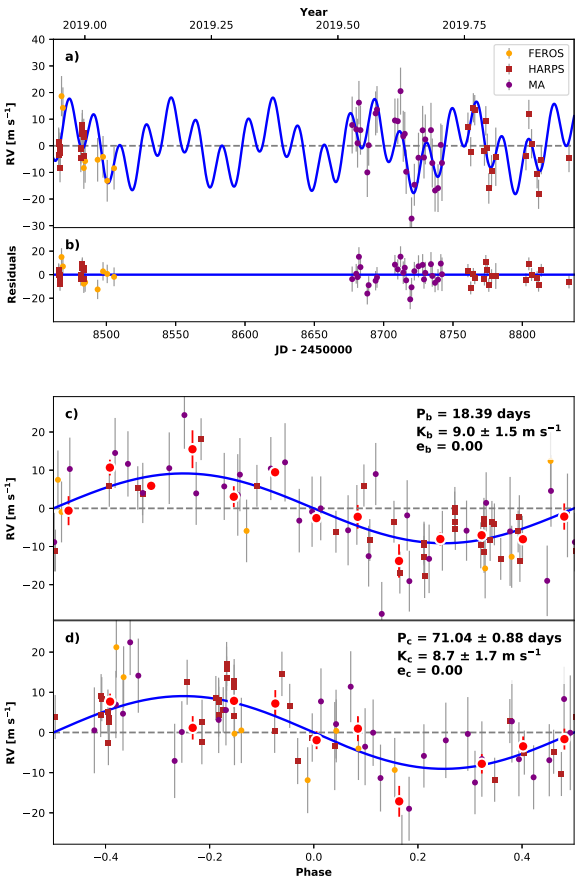

Figure 13. a) Best-fit 2-planet Keplerian orbital model for TOI-257. The maximum likelihood model(s) is plotted in blue. We add in quadrature the radial velocity jitter terms listed in Table 4 with the measurement uncertainties for all radial velocities to determine individual error bars. **b)** Residuals to the best fit 2-planet model. **c)** Same, but radial velocities phase-folded to the period of planet b. **d)** Same, but radial velocities phase-folded to the period of a possible planet c. Red circles (if present) are the individual velocities binned in 0.08 units of orbital phase.

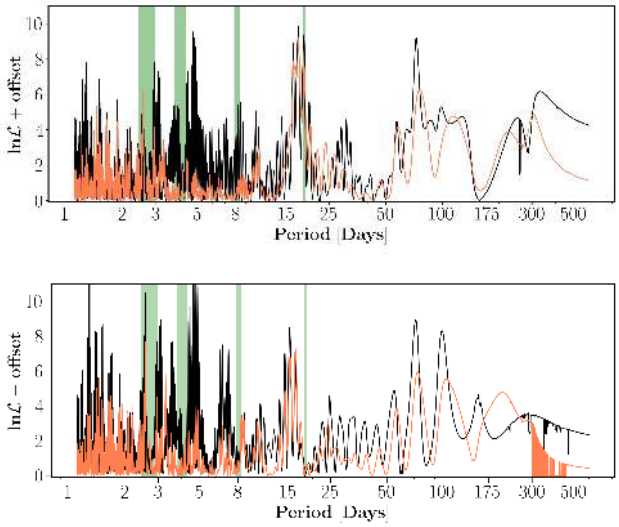

Figure 14. Log-likelihood periodograms generated using `RadVel`. Shaded from right to left are the period of planet b (insignificant width), the estimated stellar rotation period $P_{\rm rot}$ from Table 4 (width is $\pm 1\sigma$), and aliases $P_{\rm rot}/2$, $P_{\rm rot}/3$. The orange line includes a Gaussian Process (GP) to model stellar-activity with a quasi-periodic kernel with priors listed in Table 5, while the black line models remaining jitter as per-instrument Gaussian noise. **Top**: A 1-planet circular model tested at a wide range in fixed periods, fitting for K, T_c and the relative instrument dependent offsets and noise terms (or single GP). **Bottom**: Same, but for a 2-planet model assuming a fixed period and T_c for planet b from Table 4, but varying both semi-amplitudes to search for additional planets.

4 DISCUSSION

Here we have presented the discovery of TOI-257b, the first MINERVA-Australis led confirmation of a *TESS* transiting planet candidate. TOI-257b is a warm sub-Saturn planet with a radius $\sim$ 25% smaller than Saturn ($R_P = 7.02^{+0.15}_{-0.13}\ R_\oplus$) and a mass $\sim$ 55% less than Saturn ($M_P = 42.6^{+7.3}_{-7.0}\ M_\oplus$) on a moderately eccentric ($e = 0.242^{+0.040}_{-0.065}$) orbit of $P = 18.38827 \pm 0.00072$ days. The measured mass and radius give a mean density of $0.67^{+0.13}_{-0.12}$ g cm^{-3}, consistent with the density of Saturn (0.687 g cm^{-3}) and less dense than Jupiter (1.326 g cm^{-3}). Therefore, based on the mass, radius, and bulk density of this planet, it lies within the regime of planets classified as 'Neptunian worlds' by Chen & Kipping (2017). Further analysis of the radial velocity data also reveals strong evidence for a second sub-Saturn mass planet in the system with an orbit of $\sim$ 71 days. We consider this second planet as a 'statistically validated' candidate.

To understand the planet formation process, we must determine the compositions of warm sub-Saturns such as TOI-257b, a class of planet which is completely absent from the Solar System. Such objects provide important data for models studying planetary interiors because their masses are sufficiently small that their cores are not degenerate. That is, their mass and radius are dependent on each other such that the core and envelope mass fraction has a unique solution (e.g. Weiss & Marcy 2014; Petigura et al. 2016; Pepper et al. 2017; Petigura et al. 2017). For planets near the mass of Jupiter, cores are degenerate, and planetary radii are essentially independent of mass. Warm sub-Saturns represent an observational sweet

spot where mass and radius are comparatively easy to measure, and where those measurements deliver a unique solution for the planet's core/envelope mass ratio. This is particularly true for sub-Saturns with incident flux less than the $\sim 0.2\times10^9$ erg s^{-1} cm^{-2} limit where stellar irradiation can inflate planetary radii (Demory & Seager 2011). The incident flux for TOI-257b is $\sim 0.25\times10^9$ erg s^{-1} cm^{-2} and is very near this limit. Thus the effects of stellar irradiation on the radius of TOI-257b is likely negligible, allowing its internal structure to be modeled and highlights the significant value of discovering other similar planets with low incident flux.

Figure 15 shows the radius-density diagram for Neptunian worlds (similarly defined after Chen & Kipping 2017 as those with radii from $\sim 2-10\,R_\oplus$). We show those planets for which the density has been measured to a precision of better than 50%. TOI-257b has a mean density that is comparable to other exoplanets around the same size. Figure 15 also shows the apparent trend of decreasing bulk density as a function of planet radius, indicative of the increasingly large volatile gas envelope up to around the radius of Saturn.

In Figure 16 we plot the orbital period versus eccentricity for well-characterized transiting exoplanets with a measured mass from radial velocity measurements. The size of the symbols scales with $\log_{10}$ of the planet mass. TOI-257b is on an eccentric orbit of $e = 0.242^{+0.040}_{-0.065}$ and lies near the upper range of eccentricity values for other 'warm' Neptune and Jovian planets that have orbital periods of $P \geq 10$ days in this sample. Figure 16 also shows that planets on short period orbits of $P \leq 10$ days tend to have nearly circular orbits, likely due to affects of tidal interactions with the host star circularizing the orbits that were once more eccentric (Fabrycky & Tremaine 2007). For planets orbiting beyond $P \sim 10$ days, tidal effects with the host star are expected to be too weak to fully circularize the orbits and a more broad distribution of orbital eccentricity is observed.

Measurements of the spin-orbit alignment for transiting warm Neptunian and Jovian worlds via the Rossiter-McLaughlin effect can provide powerful insights into the origins and migration histories of these planets (e.g., Queloz et al. 2000; Chatterjee et al. 2008; Winn et al. 2010; Naoz et al. 2011; Addison et al. 2018; Wang et al. 2018). Both classes of planets are strongly believed to have been formed beyond their hosts' protostellar ice line and then experienced inward migration through one of two types of migration channels, quiescent migration through the disk (Lin et al. 1996) or violently dynamical high-eccentricity migration (Fabrycky & Tremaine 2007; Ford & Rasio 2008; Naoz et al. 2011). The latter migration mechanism is thought to be responsible for producing many of the known hot Jupiters due to the large observed range in their spin-orbit angles (e.g., see, Albrecht et al. 2012; Addison et al. 2013, 2018). However, it is unknown if this is the case for the warm sub-Saturn and Neptunian worlds like TOI-257b with orbits greater than 10 days. The limited sample of spin-orbit angles measured for these planet populations (only seven so far according to the TEPCat catalog[6], see Southworth 2011) makes it difficult to draw any firm conclusions and more measurements are urgently needed. This planet presents a suitable candidate for studying the spin-orbit via the Rossiter-McLaughlin effect. We predict that the radial velocity semi-amplitude of the Rossiter-McLaughlin effect for TOI-257 to be ~ 8 m s^{-1} based on the stellar and planetary parameters we obtained for this system. The predicted signal, while small, should be detectable on very high-precision (~ 1 m s^{-1}) radial velocity facilities in the south such as on HARPS (Rupprecht et al. 2004), PFS (Crane et al. 2006), and ESPRESSO (Pepe et al. 2010). We predict, given the stellar rotational velocity (as determined from the rotational period and stellar radius) is consistent with the measured $v \sin i$ from spectroscopy (i.e., suggesting that the stellar obliquity is near 90 deg), that the projected spin-orbit angle λ when measured should be close to the true spin-orbit angle ψ.

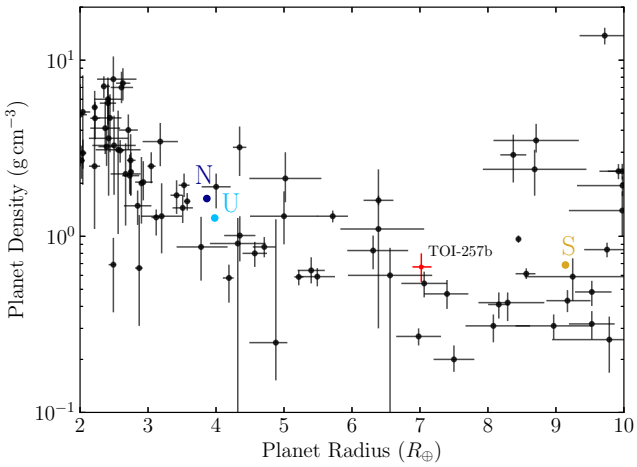

Figure 15. Planet radii versus density for Neptunian planets with $R_P = 2-10\,R_\oplus$ and that have a density measured to better than 50%. TOI-257b studied in this paper is labeled and plotted in red. The Solar System planets Saturn, Uranus, and Neptune are plotted as the gold colored letter S, light blue colored letter U, and dark blue colored letter N, respectively. Planets taken from the NASA Exoplanet Archive (https://exoplanetarchive.ipac.caltech.edu/).

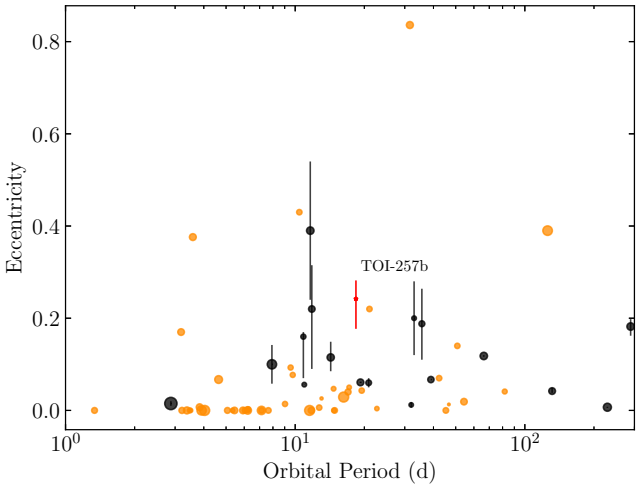

Figure 16. Orbital period versus eccentricity for well-characterized transiting exoplanets and confirmed by radial velocities. TOI-257b is labeled and plotted in red. The size of the plotted circles scales with $\log_{10}$ of the planet mass. Circles in black are those with a measured uncertainty for the eccentricity while those in orange have no reported uncertainty on the eccentricity value.

[6] https://www.astro.keele.ac.uk/jkt/tepcat/

5 CONCLUSIONS

We report the discovery of TOI-257b, a $R_P = 0.626^{+0.013}_{-0.012}$ R$_J$ ($R_P \sim 7.0$ $R_\oplus$) and $M_P = 0.134^{+0.023}_{-0.022}$ M$_J$ ($M_P \sim 42.6$ $M_\oplus$) transiting planet found by *TESS* and confirmed using radial velocity data from Minerva-Australis, FEROS, and HARPS as well as direct imaging from SOAR and Zorro. We also statistically validate an additional non-transiting long-period ($\sim$ 71 day) sub-Saturn mass planet candidate orbiting TOI-257 from analysis of the radial velocity data. TOI-257b belongs to a population of exoplanets between the sizes of Neptune and Saturn that appears to be rare. Furthermore, TOI-257b transits a very bright star ($V = 7.570$ mag) on a relatively long-period orbit of 18.423 days making it a great candidate for future follow-up observations to measure its spin-orbit alignment. Warm sub-Saturns such as TOI-257b are important population of planets to study for understanding the formation, internal structures and compositions, and evolution and migration of giant planets. Future observational work of this planetary system will help to elucidate our understanding of these rare sub-Saturn planets that are absent in the Solar System.

ACKNOWLEDGEMENTS

Minerva-Australis is supported by Australian Research Council LIEF Grant LE160100001, Discovery Grant DP180100972, Mount Cuba Astronomical Foundation, and institutional partners University of Southern Queensland, UNSW Australia, MIT, Nanjing University, George Mason University, University of Louisville, University of California Riverside, University of Florida, and The University of Texas at Austin.

We respectfully acknowledge the traditional custodians of all lands throughout Australia, and recognise their continued cultural and spiritual connection to the land, waterways, cosmos, and community. We pay our deepest respects to all Elders, ancestors and descendants of the Giabal, Jarowair, and Kambuwal nations, upon whose lands the Minerva-Australis facility at Mt Kent is situated.

B.P.B. acknowledges support from the National Science Foundation grant AST-1909209.

This research has made use of the NASA Exoplanet Archive, which is operated by the California Institute of Technology, under contract with the National Aeronautics and Space Administration under the Exoplanet Exploration Program. Funding for the *TESS* mission is provided by NASA's Science Mission directorate. We acknowledge the use of public *TESS* Alert data from pipelines at the *TESS* Science Office and at the *TESS* Science Processing Operations Center. The results reported herein benefited from collaborations and/or information exchange within NASA's Nexus for Exoplanet System Science (NExSS) research coordination network sponsored by NASA's Science Mission Directorate. Based on observations obtained at the Gemini Observatory, which is operated by the Association of Universities for Research in Astronomy, Inc., under a cooperative agreement with the NSF on behalf of the Gemini partnership: the National Science Foundation (United States), National Research Council (Canada), CONICYT (Chile), Ministerio de Ciencia, Tecnología e Innovación Productiva (Argentina), Ministério da Ciência, Tecnologia e Inovação (Brazil), and Korea Astronomy and Space Science Institute (Republic of Korea). Some of the Observations in the paper made use of the High-Resolution Imaging instrument Zorro at Gemini-South. Zorro was funded by the NASA Exoplanet Exploration Program and built at the NASA Ames Research Center by Steve B. Howell, Nic Scott, Elliott P. Horch, and Emmett Quigley.

D.H. acknowledges support by the National Aeronautics and Space Administration through the *TESS* Guest Investigator Program (80NSSC18K1585) and by the National Science Foundation (AST-1717000). A.C. acknowledges support by the National Science Foundation under the Graduate Research Fellowship Program. W.J.C., W.H.B., M.B.N. and A.M. acknowledge support from the Science and Technology Facilities Council and UK Space Agency. Funding for the Stellar Astrophysics Centre is provided by The Danish National Research Foundation (Grant DNRF106). R.B. acknowledges support from FONDECYT Post-doctoral Fellowship Project 3180246, and from the Millennium Institute of Astrophysics (MAS). H.Z. Hui Zhang is supported by the Natural Science Foundation of China (NSFC grants 11673011, 11933001). A.J. acknowledges support from FONDECYT project 1171208 and by the Ministry for the Economy, Development, and Tourism's Programa Iniciativa Científica Milenio through grant IC 120009, awarded to the Millennium Institute of Astrophysics (MAS). A.M.S. is pastially supported by grants ESP2017-82674-R (Spanish Government) and 2017-SGR-1131 (Generalitat de Catalunya). A.M. acknowledges support from the ERC Consolidator Grant funding scheme (project ASTEROCHRONOMETRY, G.A. n. 772293). R.A.G. acknowledge the support of the PLATO grant from the CNES. S.M. acknowledges support from the European Research Council through the SPIRE grant 647383. T.L.C. acknowledges support from the European Union's Horizon 2020 research and innovation programme under the Marie Skłodowska-Curie grant agreement No. 792848 (PULSATION). This work was supported by FCT/MCTES through national funds (UID/FIS/04434/2019). E.C. is funded by the European UnionâĂŹs Horizon 2020 research and innovation program under the Marie Sklodowska-Curie grant agreement No. 664931. V.S.A. acknowledges support from the Independent Research Fund Denmark (Research grant 7027-00096B). S.B. acknowledges NASA grant NNX16AI09G and NSF grant AST-1514676. I.J.M.C. acknowledges support from the NSF through grant AST-1824644, and from NASA through Caltech/JPL grant RSA-1610091. T.D. acknowledges support from MITâĂŹs Kavli Institute as a Kavli postdoctoral fellow. D.B. acknowledges support from NASA through the TESS GI program (80NSSC19K0385). C.K. acknowledges support by Erciyes University Scientific Research Projects Coordination Unit under grant number #9749.

Software: Astropy (Astropy Collaboration et al. 2018), Matplotlib (Hunter 2007), DIAMONDS (Corsaro & De Ridder 2014), isoclassify (Huber et al. 2017), `EXOFASTv2` (Eastman et al. 2013; Eastman 2017; Eastman et al. 2019)

REFERENCES

Adams F. C., Laughlin G., 2006, ApJ, 649, 1004
Addison B. C., Tinney C. G., Wright D. J., Bayliss D., Zhou G., Hartman J. D., Bakos G. Á., Schmidt B., 2013, ApJ, 774, L9
Addison B. C., Wang S., Johnson M. C., Tinney C. G., Wright D. J., Bayliss D., 2018, AJ, 156, 197
Addison B., et al., 2019, PASP, 131, 115003
Akaike H., 1974, IEEE Transactions on Automatic Control, 19, 716
Albrecht S., et al., 2012, ApJ, 757, 18
Anglada-Escudé G., Butler R. P., 2012, ApJS, 200, 15
Angus R., Morton T., Aigrain S., Foreman-Mackey D., Rajpaul V., 2018, MNRAS, 474, 2094
Asplund M., Grevesse N., Sauval A. J., Scott P., 2009, ARA&A, 47, 481
Astropy Collaboration et al., 2018, AJ, 156, 123

Barclay T., Pepper J., Quintana E. V., 2018, ApJS, 239, 2
Barnes S. I., Gibson S., Nield K., Cochrane D., 2012, KiwiSpec - an advanced spectrograph for high resolution spectroscopy: optical design and variations. p. 844688, doi:10.1117/12.926527
Bayliss D., et al., 2013, AJ, 146, 113
Benomar O., Baudin F., Chaplin W. J., Elsworth Y., Appourchaux T., 2012, MNRAS, 420, 2178
Blanco-Cuaresma S., 2019, MNRAS, 486, 2075
Blanco-Cuaresma S., Soubiran C., Heiter U., Jofré P., 2014, A&A, 569, A111
Boisvert J. H., Nelson B. E., Steffen J. H., 2018, MNRAS, 480, 2846
Brahm R., et al., 2016, AJ, 151, 89
Brahm R., Jordán A., Espinoza N., 2017, PASP, 129, 034002
Burnham K. P., Anderson D. R., 2002, Model Selection and Multimodel Inference. Springer
Butler R. P., Marcy G. W., Williams E., Hauser H., Shirts P., 1997, ApJ, 474, L115
Campante T. L., 2018, in Campante T. L., Santos N. C., Monteiro M. J. P. F. G., eds, Vol. 49, Asteroseismology and Exoplanets: Listening to the Stars and Searching for New Worlds. p. 55 (arXiv:1711.01959), doi:10.1007/978-3-319-59315-9_3
Chaplin W. J., Elsworth Y., Davies G. R., Campante T. L., Handberg R., Miglio A., Basu S., 2014, MNRAS, 445, 946
Chatterjee S., Ford E. B., Matsumura S., Rasio F. A., 2008, ApJ, 686, 580
Chen J., Kipping D., 2017, ApJ, 834, 17
Choi J., Dotter A., Conroy C., Cantiello M., Paxton B., Johnson B. D., 2016a, ApJ, 823, 102
Choi J., Dotter A., Conroy C., Cantiello M., Paxton B., Johnson B. D., 2016b, ApJ, 823, 102
Christensen-Dalsgaard J., 2008, Ap&SS, 316, 13
Corsaro E., De Ridder J., 2014, A&A, 571, A71
Crane J. D., Shectman S. A., Butler R. P., 2006, in Proc. SPIE. p. 626931, doi:10.1117/12.672339
Cutri R. M., et al. 2013, VizieR Online Data Catalog, p. II/328
Cutri R. M., et al., 2003, VizieR Online Data Catalog, p. II/246
Dai F., et al., 2017, AJ, 154, 226
Davies G. R., Miglio A., 2016, Astronomische Nachrichten, 337, 774
Dawson R. I., et al., 2019, AJ, 158, 65
Demarque P., Guenther D. B., Li L. H., Mazumdar A., Straka C. W., 2008, Ap&SS, 316, 31
Demory B.-O., Seager S., 2011, ApJS, 197, 12
Donati J. F., Collier Cameron A., 1997, MNRAS, 291, 1
Dotter A., 2016, ApJS, 222, 8
Eastman J., 2017, EXOFASTv2: Generalized publication-quality exoplanet modeling code, Astrophysics Source Code Library (ascl:1710.003)
Eastman J., Gaudi B. S., Agol E., 2013, PASP, 125, 83
Eastman J. D., et al., 2019, arXiv e-prints, p. arXiv:1907.09480
Fabrycky D., Tremaine S., 2007, ApJ, 669, 1298
Feroz F., Hobson M. P., Bridges M., 2009, MNRAS, 398, 1601
Figueira P., Santos N. C., Pepe F., Lovis C., Nardetto N., 2013, A&A, 557, A93
Ford E. B., Rasio F. A., 2008, ApJ, 686, 621
Foreman-Mackey D., Morton T. D., Hogg D. W., Agol E., Schölkopf B., 2016, AJ, 152, 206
Fulton B. J., Petigura E. A., Blunt S., Sinukoff E., 2018, PASP, 130, 044504
Gaia Collaboration et al., 2018a, A&A, 616, A1
Gaia Collaboration et al., 2018b, A&A, 616, A1
García R. A., Ballot J., 2019, Living Reviews in Solar Physics, 16, 4
García Saravia Ortiz de Montellano A., Hekker S., Themeßl N., 2018, MNRAS, 476, 1470
Giles H. A. C., Collier Cameron A., Haywood R. D., 2017, MNRAS, 472, 1618
Gray D. F., 2005, The Observation and Analysis of Stellar Photospheres
Gray R. O., Corbally C. J., 1994, AJ, 107, 742
Gustafsson B., Edvardsson B., Eriksson K., Jørgensen U. G., Nordlund Å., Plez B., 2008, A&A, 486, 951
Handberg R., Lund M. N., 2014, MNRAS, 445, 2698
Haywood R. D., et al., 2018, AJ, 155, 203
Heiter U., et al., 2015, Phys. Scr., 90, 054010
Høg E., et al., 2000, A&A, 355, L27
Howard A. W., et al., 2010, Science, 330, 653
Howard A. W., et al., 2012, ApJS, 201, 15
Howell S. B., Everett M. E., Sherry W., Horch E., Ciardi D. R., 2011, AJ, 142, 19
Huang C. X., et al., 2018, arXiv e-prints, p. arXiv:1807.11129
Huber D., Stello D., Bedding T. R., Chaplin W. J., Arentoft T., Quirion P.-O., Kjeldsen H., 2009, Communications in Asteroseismology, 160, 74
Huber D., et al., 2011, ApJ, 731, 94
Huber D., et al., 2017, ApJ, 844, 102
Hunter J. D., 2007, Computing In Science & Engineering, 9, 90
Jenkins J. M., et al., 2016, in Proc. SPIE. p. 99133E, doi:10.1117/12.2233418
Kallinger T., et al., 2012, A&A, 541, A51
Kaufer A., Stahl O., Tubbesing S., Nørregaard P., Avila G., Francois P., Pasquini L., Pizzella A., 1999, The Messenger, 95, 8
Kinemuchi K., Barclay T., Fanelli M., Pepper J., Still M., Howell S. B., 2012, PASP, 124, 963
Kipping D., Nesvorný D., Hartman J., Torres G., Bakos G., Jansen T., Teachey A., 2019, MNRAS, 486, 4980
Lamm M. H., Bailer-Jones C. A. L., Mundt R., Herbst W., Scholz A., 2004, A&A, 417, 557
Lee E. J., Chiang E., Ferguson J. W., 2018, MNRAS, 476, 2199
Lin D. N. C., Bodenheimer P., Richardson D. C., 1996, Nature, 380, 606
Lissauer J. J., 1993, ARA&A, 31, 129
Lund M. N., Handberg R., Davies G. R., Chaplin W. J., Jones C. D., 2015, ApJ, 806, 30
Lund M. N., Handberg R., Kjeldsen H., Chaplin W. J., Christensen-Dalsgaard J., 2017, in European Physical Journal Web of Conferences. p. 01005 (arXiv:1610.02702), doi:10.1051/epjconf/201716001005
Mathur S., et al., 2010, A&A, 511, A46
Mayor M., Queloz D., 1995, Nature, 378, 355
Mayor M., et al., 2003, The Messenger, 114, 20
McQuillan A., Aigrain S., Mazeh T., 2013, MNRAS, 432, 1203
Messina S., Desidera S., Turatto M., Lanzafame A. C., Guinan E. F., 2010, A&A, 520, A15
Montet B. T., et al., 2015, ApJ, 809, 25
Morton T. D., 2015, isochrones: Stellar model grid package (ascl:1503.010)
Mosser B., et al., 2012, A&A, 537, A30
Naoz S., Farr W. M., Lithwick Y., Rasio F. A., Teyssandier J., 2011, Nature, 473, 187
Nava C., Lopez-Morales M., Haywood R., Giles H., 2019, in AAS/Division for Extreme Solar Systems Abstracts. p. 303.13
Nielsen L. D., et al., 2019, A&A, 623, A100
Paxton B., Bildsten L., Dotter A., Herwig F., Lesaffre P., Timmes F., 2011, ApJS, 192, 3
Paxton B., et al., 2013, ApJS, 208, 4
Paxton B., et al., 2015, ApJS, 220, 15
Pepe F. A., et al., 2010, in Ground-based and Airborne Instrumentation for Astronomy III. p. 77350F, doi:10.1117/12.857122
Pepper J., et al., 2017, AJ, 153, 215
Petigura E. A., Howard A. W., Marcy G. W., 2013, Proceedings of the National Academy of Science, 110, 19273
Petigura E. A., et al., 2016, ApJ, 818, 36
Petigura E. A., et al., 2017, AJ, 153, 142
Pollack J. B., Hubickyj O., Bodenheimer P., Lissauer J. J., Podolak M., Greenzweig Y., 1996, Icarus, 124, 62
Queloz D., Eggenberger A., Mayor M., Perrier C., Beuzit J. L., Naef D., Sivan J. P., Udry S., 2000, A&A, 359, L13
Queloz D., et al., 2009, A&A, 506, 303
Quinn S. N., et al., 2019, AJ, 158, 177
Rafikov R. R., 2006, ApJ, 648, 666
Rajpaul V., Aigrain S., Osborne M. A., Reece S., Roberts S., 2015, MNRAS, 452, 2269
Ricker G. R., et al., 2015, Journal of Astronomical Telescopes, Instruments, and Systems, 1, 014003
Rodrigues T. S., et al., 2014, MNRAS, 445, 2758
Rodrigues T. S., et al., 2017, MNRAS, 467, 1433

Rupprecht G., et al., 2004, in Moorwood A. F. M., Iye M., eds, Society of Photo-Optical Instrumentation Engineers (SPIE) Conference Series Vol. 5492, Proc. SPIE. pp 148–159, doi:10.1117/12.551267
Scargle J. D., 1982, ApJ, 263, 835
Schlafly E. F., Finkbeiner D. P., 2011, ApJ, 737, 103
Schofield M., et al., 2019, ApJS, 241, 12
Serenelli A., et al., 2017, ApJS, 233, 23
Silva Aguirre V., et al., 2015, MNRAS, 452, 2127
Southworth J., 2011, MNRAS, 417, 2166
Stassun K. G., Torres G., 2018, ApJ, 862, 61
Stassun K. G., et al., 2019, AJ, 158, 138
Stello D., et al., 2009, ApJ, 700, 1589
Sullivan P. W., et al., 2015, ApJ, 809, 77
Tanigawa T., Ikoma M., 2007, ApJ, 667, 557
Tokovinin A., 2018, PASP, 130, 035002
Trifonov T., et al., 2017, A&A, 602, L8
Twicken J. D., Clarke B. D., Bryson S. T., Tenenbaum P., Wu H., Jenkins J. M., Girouard F., Klaus T. C., 2010, Photometric analysis in the Kepler Science Operations Center pipeline. p. 774023, doi:10.1117/12.856790
Van Eylen V., et al., 2018, MNRAS, 478, 4866
Vanderburg A., et al., 2016a, ApJS, 222, 14
Vanderburg A., Plavchan P., Johnson J. A., Ciardi D. R., Swift J., Kane S. R., 2016b, MNRAS, 459, 3565
Vanderburg A., et al., 2019, ApJ, 881, L19
Wang S., Addison B., Fischer D. A., Brewer J. M., Isaacson H., Howard A. W., Laughlin G., 2018, AJ, 155, 70
Wang S., et al., 2019, AJ, 157, 51
Weidenschilling S. J., 2005, Space Sci. Rev., 116, 53
Weiss L. M., Marcy G. W., 2014, ApJ, 783, L6
Weiss W. W., Moffat A. F. J., Kudelka O., 2008, Communications in Asteroseismology, 157, 271
Winn J. N., Fabrycky D., Albrecht S., Johnson J. A., 2010, ApJ, 718, L145
Wittenmyer R. A., et al., 2013, ApJS, 208, 2
Wittenmyer R. A., Horner J., Carter B. D., Kane S. R., Plavchan P., Ciardi D., MINERVA-Australis consortium t., 2018, arXiv e-prints, p. arXiv:1806.09282
Wittenmyer R. A., Bergmann C., Horner J., Clark J., Kane S. R., 2019, MNRAS, 484, 4230
Wittenmyer R. A., et al., 2020, MNRAS, 492, 377
Wright J. T., Marcy G. W., Howard A. W., Johnson J. A., Morton T. D., Fischer D. A., 2012, ApJ, 753, 160
Zhou G., et al., 2019, AJ, 158, 141
Ziegler C., Tokovinin A., Briceño C., Mang J., Law N., Mann A. W., 2020, AJ, 159, 19

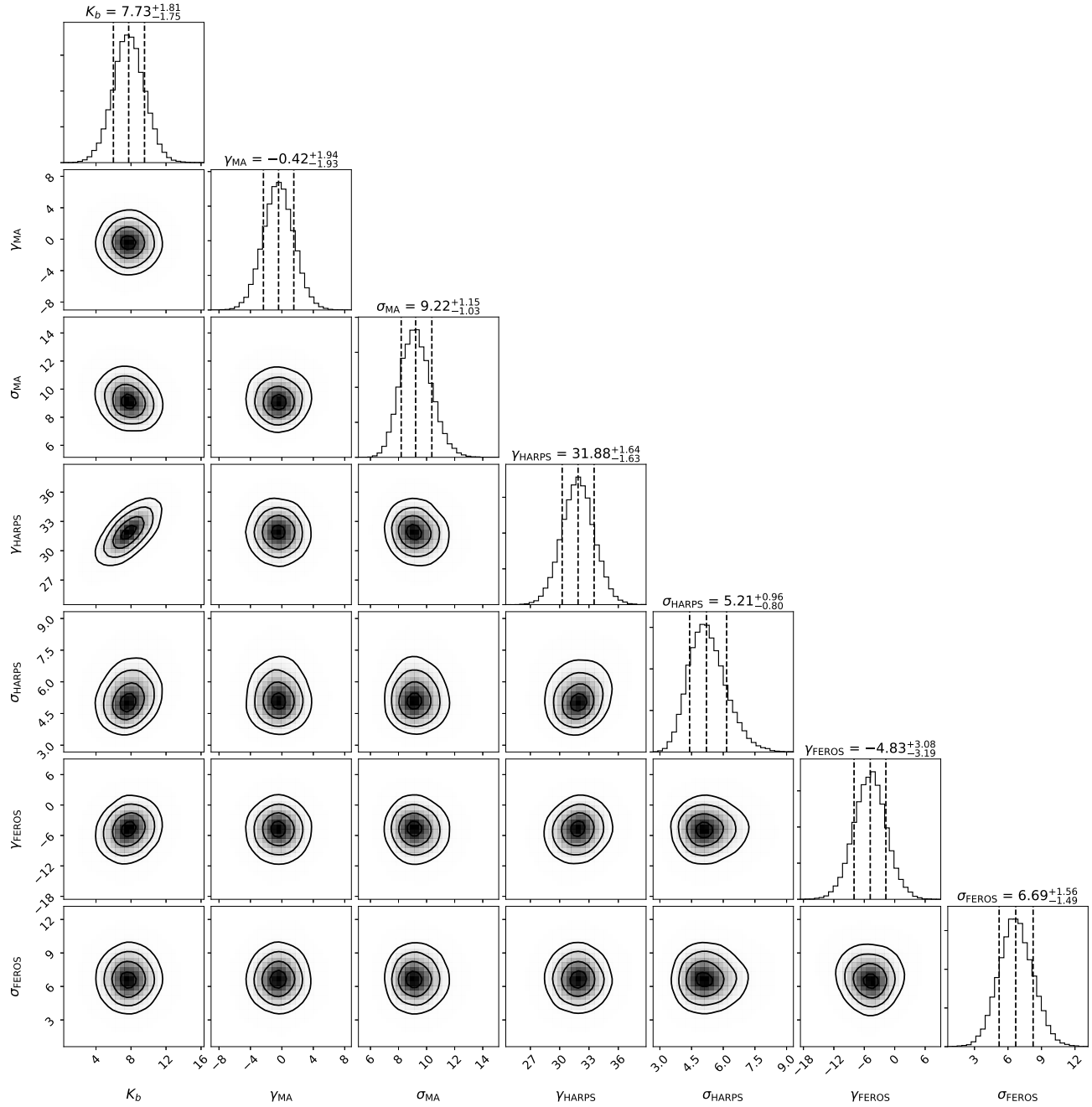

Figure A1. Posterior distributions from `RadVel` for all parameters for a 1-planet circular model.

APPENDIX A: `RADVEL` POSTERIOR DISTRIBUTION PLOTS

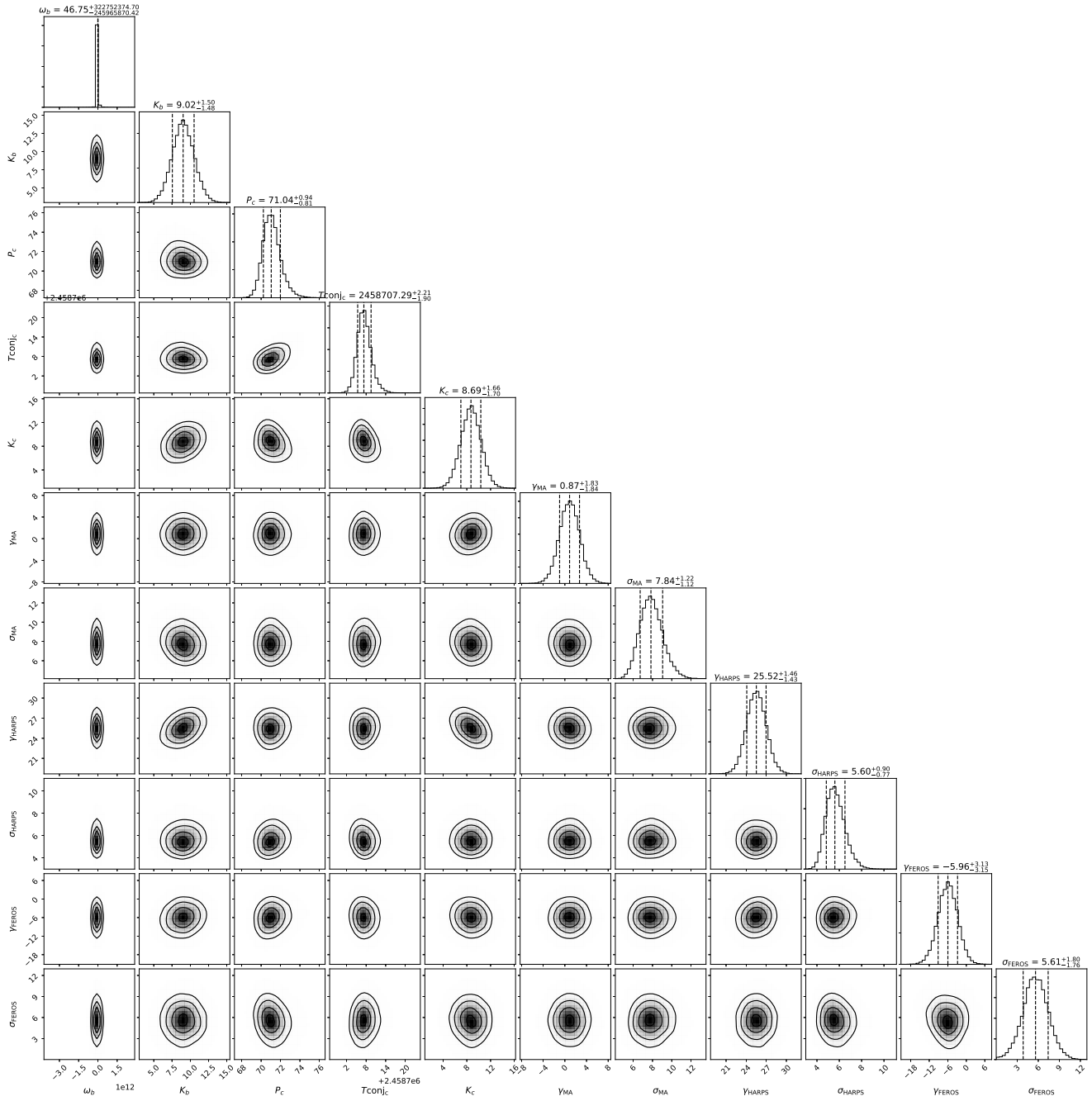

Figure A2. Same as Fig. A1, but for a 2-planet circular model.

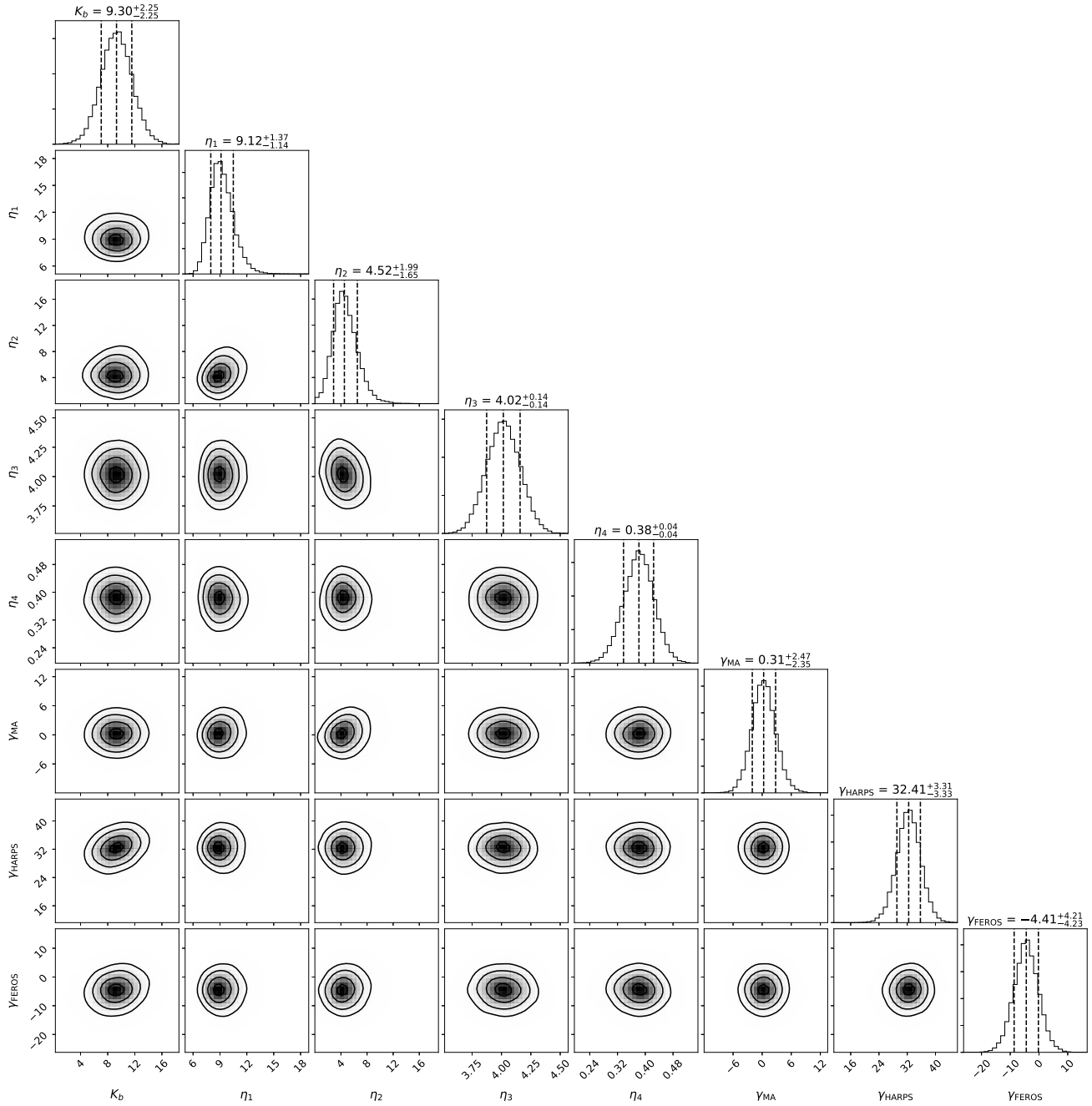

Figure A3. Posterior distributions for all parameters for a 1-planet circular model in `RadVel` with a quasi-periodic Gaussian Process to model stellar-activity. Priors for hyper-parameters are provided in Table 5.

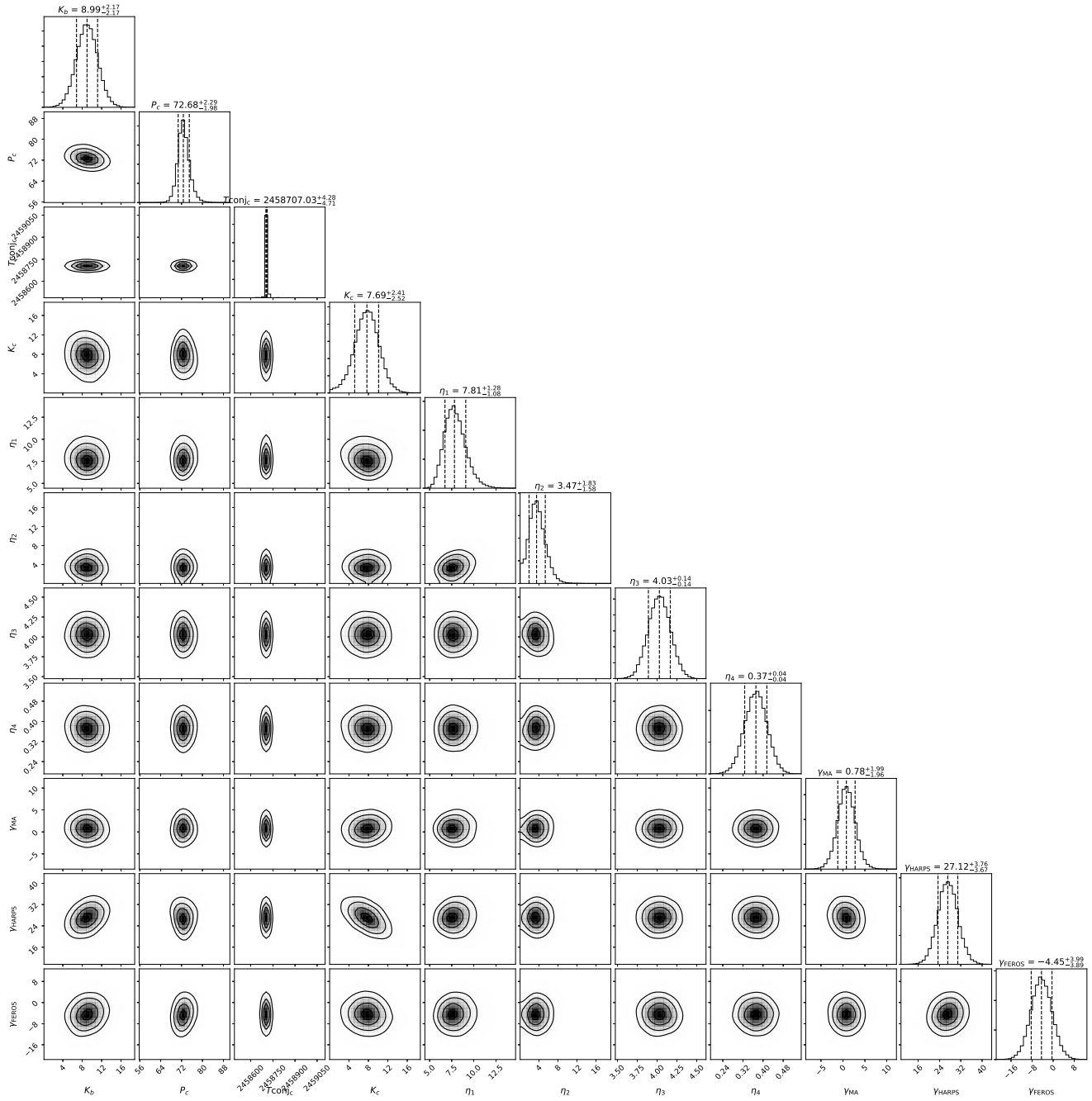

Figure A4. Same as Fig. A3, but for a 2-planet circular model.

APPENDIX B: AUTHOR AFFILIATIONS

[1]University of Southern Queensland, Centre for Astrophysics, West Street, Toowoomba, QLD 4350 Australia
[2]Sub-department of Astrophysics, Department of Physics, University of Oxford, Denys Wilkinson Building, Keble Road, Oxford, OX1 3RH, UK
[3]Department of Physics & Astronomy, George Mason University, 4400 University Drive MS 3F3, Fairfax, VA 22030, USA
[4]Department of Earth and Planetary Sciences, University of California, Riverside, CA 92521, USA
[5]Institute for Astronomy, University of Hawai'i, 2680 Woodlawn Drive, Honolulu, HI 96822, USA
[6]Department of Astronomy, The University of Texas at Austin, Austin, TX 78712, USA
[7]NASA Sagan Fellow
[8]School of Physics and Astronomy, University of Birmingham, Birmingham B15 2TT, UK
[9]Stellar Astrophysics Centre (SAC), Department of Physics and Astronomy, Aarhus University, Ny Munkegade 120, DK-8000 Aarhus C, Denmark
[10]NSF Graduate Research Fellow
[11]Center for Astrophysics, Harvard & Smithsonian, 60 Garden St., Cambridge, MA 02138, USA
[12]Dunlap Institute for Astronomy and Astrophysics, University of Toronto, 50 St. George Street, Toronto, Ontario M5S 3H4, Canada
[13]Center of Astro-Engineering UC, Pontificia Universidad Católica de Chile, Av. Vicuña Mackenna 4860, 7820436 Macul, Santiago, Chile
[14]Instituto de Astrofísica, Pontificia Universidad Católica de Chile, Av. Vicuña Mackenna 4860, Macul, Santiago, Chile
[15]Millennium Institute for Astrophysics, Chile
[16]Space Telescope Science Institute, 3700 San Martin Drive, Baltimore, MD 21218, USA
[18]Department of Physics and Astronomy, University of Louisville, Louisville, KY 40292, USA
[19]Department of Physical Sciences, Kutztown University, Kutztown, PA 19530, USA
[20]Vanderbilt University, Department of Physics & Astronomy, 6301 Stevenson Center Ln., Nashville, TN 37235, USA
[21]Fisk University, Department of Physics, 1000 18th Ave. N., Nashville, TN 37208, USA
[22]Sydney Institute for Astronomy (SIfA), School of Physics, University of Sydney, 2006, Australia
[24]Department of Physics, Westminster College, 319 South Market Street, New Wilmington, PA 16172, USA
[25]Dept. of Physics and Astronomy, University of Kansas, 1251 Wescoe Hall Dr.,Lawrence, KS 66045, USA
[26]Department of Physics, Massachusetts Institute of Technology, Cambridge, MA, USA
[27]Department of Astronomy, Yale University, New Haven, CT 06511, USA
[28]Space Science & Astrobiology Division, NASA Ames Research Center, Moffett Field, CA 94035, USA
[29]Department of Physics and Astronomy, The University of North Carolina at Chapel Hill, Chapel Hill, NC 27599-3255, USA
[31]Department of Physics and Kavli Institute for Astrophysics and Space Research, Massachusetts Institute of Technology, Cambridge, MA 02139, USA
[32]Kavli Fellow
[33]Exoplanetary Science at UNSW, School of Physics, UNSW Sydney, NSW 2052, Australia
[34]*51 Pegasi b* Fellow
[35]School of Astronomy and Space Science, Key Laboratory of Modern Astronomy and Astrophysics in Ministry of Education, Nanjing University, Nanjing 210046, Jiangsu, China
[36]Max-Planck-Institut für Astronomie, Königstuhl 17, Heidelberg 69117, Germany
[37]Harvard-Smithsonian Center for Astrophysics, 60 Garden St, Cambridge, MA 02138, USA
[38]Earth and Planetary Sciences, Massachusetts Institute of Technology, 77 Massachusetts Avenue, Cambridge, MA 02139, USA
[39]Department of Astrophysical Sciences, Princeton University, 4 Ivy Lane, Princeton, NJ 08544, USA
[40]NASA Ames Research Center, Moffett Field, CA 94035, USA
[41]School of Physical Sciences, The Open University, Milton Keynes MK7 6AA, UK
[42]Department of Physics, Lehigh University, 16 Memorial Drive East, Bethlehem, PA 18015, USA
[43]Exoplanets and Stellar Astrophysics Laboratory, Mail Code 667, NASA Goddard Space Flight Center, Greenbelt, MD 20771, USA
[44]Perth Exoplanet Survey Telescope, Perth, Western Australia
[45]Center for Space Science, NYUAD Institute, New York University Abu Dhabi, PO Box 129188, Abu Dhabi, United Arab Emirates
[46]Dept. of Chemistry & Physics, Florida Gulf Coast University, 10501 FGCU Blvd. S., Fort Myers, FL 33965 USA
[47]Instituto de Astrofísica e Ciências do Espaço, Universidade do Porto, CAUP, Rua das Estrelas, 4150-762 Porto, Portugal
[48]Departamento de Física e Astronomia, Faculdade de Ciências da Universidade do Porto, Rua do Campo Alegre, s/n, PT4169-007 Porto, Portugal
[49]INAF - Osservatorio Astrofisico di Catania, via S. Sofia 78, 95123, Catania, Italy
[50]Instituto de Astrofísica de Canarias (IAC), 38205 La Laguna, Tenerife, Spain
[51]Universidad de La Laguna (ULL), Departamento de Astrofísica, E-38206 La Laguna, Tenerife, Spain
[53]IRFU, CEA, Université Paris-Saclay, F-91191 Gif-sur-Yvette, France
[54]AIM, CEA, CNRS, Université Paris-Saclay, Université Paris Diderot, Sorbonne Paris Cité, F-91191 Gif-sur-Yvette, France
[55]Center for Exoplanets and Habitable Worlds, Department of Astronomy & Astrophysics, 525 Davey Laboratory, The Pennsylvania State University, University Park, PA 16802, USA
[56]Max-Planck-Institut für Sonnensystemforschung, Justus-von-Liebig-Weg 3, 37077 Göttingen, Germany
[57]Institute of Astrophysics, University of Vienna, 1180 Vienna, Austria
[58]Department of Physics and Astronomy, Iowa State University, Ames, IA 50011 USA
[59]Department of Astronomy & Space Sciences, Erciyes University, Kayseri, Turkey
[60]LESIA, Observatoire de Paris, Université PSL, CNRS, Sorbonne Université, Université de Paris, 92195 Meudon, France
[61]Institute of Space Sciences (ICE, CSIC) Campus UAB, Carrer de Can Magrans, s/n, E-08193, Barcelona, Spain
[62]Institut dâĂŹEstudis Espacials de Catalunya (IEEC), C/Gran Capita, 2-4, E-08034, Barcelona, Spain

This paper has been typeset from a TEX/LATEX file prepared by the author.